Five new eclipsing binaries with low-mass companions

(article starts on next page)

Astronomy & Astrophysics

Five new eclipsing binaries with low-mass companions

J. Lipták[1,2,*], M. Skarka[1,4], E. Guenther[3], P. Chaturvedi[3], M. Vítková[1,4], R. Karjalainen[1], J. Šubjak[1,9], A. Hatzes[3], A. Bieryla[9], D. Gandolfi[10], S. H. Albrecht[13], P. G. Beck[5,6], H. J. Deeg[5,6], M. E. Everett[8], J. Higuera[8], D. Jones[5,6,7], S. Mathur[5,6], Y. G. Patel[8], C. M. Persson[11], S. Redfield[12], and P. Kabáth[1]

[1] Astronomical Institute, Academy of Sciences, Fričova 298, 251 65 Ondřejov, Czech Republic
[2] Astronomical Institute, Faculty of Mathematics and Physics, Charles University, V Holešovičkách 2, 180 00 Praha 8, Czech Republic
[3] Thüringer Landessternwarte Tautenburg, Sternwarte 5, 07778 Tautenburg, Germany
[4] Department of Theoretical Physics and Astrophysics, Faculty of Science, Masaryk University, Kotlářská 267/2, 611 37 Brno, Czech Republic
[5] Instituto de Astrofísica de Canarias, E-38205 La Laguna, Tenerife, Spain
[6] Departamento de Astrofísica, Universidad de La Laguna, E-38206 La Laguna, Tenerife, Spain
[7] Nordic Optical Telescope, Rambla José Ana Fernández Pérez 7, 38711 Breña Baja, Spain
[8] NSF's National Optical-Infrared Astronomy Research Laboratory, 950 N. Cherry Ave., Tucson, AZ 85719, USA
[9] Center for Astrophysics | Harvard & Smithsonian, 60 Garden Street, Cambridge, MA 02138, USA
[10] Dipartimento di Fisica, Università di Torino, Via P. Giuria 1, 10125 Torino, Italy
[11] Department of Space, Earth and Environment, Chalmers University of Technology, Onsala Space Observatory, SE-439 92 Onsala, Sweden
[12] Astronomy Department and Van Vleck Observatory, Wesleyan University, Middletown, CT 06459, USA
[13] Stellar Astrophysics Centre, Department of Physics and Astronomy, Aarhus University, Ny Munkegade 120, DK-8000 Aarhus C, Denmark

ABSTRACT

Precise space-based photometry from the Transiting Exoplanet Survey Satellite results in a huge number of exoplanetary candidates. However, the masses of these objects are unknown and must be determined by ground-based spectroscopic follow-up observations, frequently revealing the companions to be low-mass stars rather than exoplanets. We present the first orbital and stellar parameter solutions for five such eclipsing binary-star systems using radial-velocity follow-up measurements together with spectral-energy-distribution solutions. TOI-416 and TOI-1143 are totally eclipsing F+M star systems with well-determined secondary masses, radii, and temperatures. TOI-416 is a circular system with an F6 primary and a secondary with a mass of $M_2 = 0.131(8)\,M_\odot$. TOI-1143 consists of an F6 primary with an $M_2 = 0.142(3)\,M_\odot$ secondary on an eccentric orbit with a third companion. With respect to the other systems, TOI-1153 shows ellipsoidal variations, TOI-1615 contains a pulsating primary, and TOI-1788 has a spotted primary, while all have moderate mass ratios of 0.2–0.4. However, these systems are in a grazing configuration, which limits their full description. The parameters of TOI-416B and TOI-1143B are suitable for the calibration of the radius-mass relation for dwarf stars.

Key words. techniques: radial velocities – binaries: eclipsing – stars: fundamental parameters – stars: low-mass

1. Introduction

Dwarf stars of spectral type M are the most common in the Galaxy. With masses of $M < 0.6\,M_\odot$ and above the hydrogen burning limit of $M = 0.075\,M_\odot$ (Chabrier et al. 2023), they comprise up to ≈40% of the entire stellar population assuming initial mass-function by Chabrier (2003). However, our knowledge of their fundamental parameters is still limited. To estimate the masses of single M dwarfs, one needs to use stellar structure models. The only quantities directly related to the observations are the effective temperature and stellar radius derived from the spectral energy distribution (SED) of dwarfs with measured parallaxes and metalicity, and surface gravity derived from spectroscopy. However, the precision of the surface gravities determined in this way is on the order of 10–15% at best, which is not low enough to constrain the mass well.

The physics of stellar modeling of low-mass stars is challenging. These stars are dominated by convection; stars with masses $\lesssim 0.35\,M_\odot$, are fully convective according to Chabrier & Baraffe (1997). This, together with the rotation of the stars, generates magnetic fields. Further complication comes from the boundary conditions - cold atmospheres contain molecular species with many transitions contributing significantly to the opacity. For the calibration of these models, we need observations with sufficiently small uncertainties on the masses and radii. The only source of mass estimates that are independent of stellar structure models are binary stars, either astrometric or eclipsing, where we can obtain the secondary mass from radial velocities. In the case of a purely spectroscopic binary (i.e., not eclipsing), we can only determine $M_2 \sin i$, where i is the inclination of the binary orbit.

Before 2010, only about a dozen M dwarfs with masses and radii with levels of precisions better than 10% were known, usually M+M systems close to Earth such as CU Cnc (Ribas 2003). Subsequently, space-based exoplanetary missions came to the rescue. The eclipse depth of an M dwarf star orbiting an early-type star is quite similar to a brown dwarf or a hot

Jupiter orbiting a G, K, or M star. Thus, the mission pipelines were automatically identifying these systems. Further spectroscopic follow-up is needed to discern the cases based on radial-velocity amplitudes. This led to an increase in interest. The number of these binary systems is steadily growing, with the current count being just below 100 thanks to works such as the EBLM (eclipsing binary-low mass) project (Triaud et al. 2013), Maxted et al. (2023) using WASP and Kepler candidates, Chaturvedi et al. (2018) using different photometry sources, and Alton & Stępień (2018) studying contact binary systems and others. These new data started to show systematic deviations from the models of Baraffe et al. (2015) or MIST (Choi et al. 2016). For a given mass, the observational radii are around 5% bigger, and temperatures are around 100 K colder than expected, as was shown in works of Parsons et al. (2018), Duck et al. (2023), and Wanderley et al. (2023). Also, there is a larger scatter in the radius–mass relation than expected, suggesting that magnetic fields, rotation, and detailed chemical composition may play a role that is not well described by the models.

Most stars in the Galaxy form with companions. About half of all main-sequence stars of spectral classes F and G have smaller companions, with about half of those being close binaries (with $a < 10$ au) as is shown in the review on stellar multiplicity by Offner et al. (2023). Concerning the orbital eccentricities of the close binaries, the internal structure of stars is important. Stars below the Kraft break ($M \approx 1.3\,M_\odot$) (Kraft 1967) with convective zones in their interior are expected to be circularized below $P = 8$ days in comparison with hotter, radiative-envelope stars that tend to have circular orbits only below $P = 2$ days (Offner et al. 2023). Among solar type stars, the distribution of mass ratios is quite uniform, except for the overabundance of twin systems and the low-mass cut-off at brown dwarf masses. This underabundance of close brown-dwarf companions was described by Campbell et al. (1988) and is commonly called the brown-dwarf desert. The most probable cause is a difference in the mechanisms that drive the formation of close stellar companions (disk fragmentation) and planets (core accretion) that likely overlap in the brown-dwarf mass range. More recently, the imaging survey by Duchêne et al. (2023) extended the brown-dwarf desert to an absence of low-mass stellar companions to late B- and A-type stars (albeit just in wide binaries), suggesting that the processes are mostly invariant of primary mass and driven by mass ratio (q) instead, with a truncation of companion distribution at $q = 0.075$.

Here, we present the characterization of five systems identified as exoplanetary candidates via the Transiting Exoplanet Survey Satellite (TESS) mission that turned out to be eclipsing binaries with low-mass stellar companions. TOI-416 and TOI-1143 are well-described systems comprising F-type primaries and late M-dwarf secondaries. These are TOI-1615 – an M dwarf secondary at the convective-radiative core transition orbiting around a δ Scuti variable, and TOI-1153 and TOI-1788, which are are systems with secondaries of late-K and mid-M spectral type for which the description is somewhat limited by the grazing nature of the eclipses.

2. Observations

Our targets were identified as exoplanetary candidates in TESS space-based photometry between January 2019 and March 2020. We contributed to the ground-based spectroscopic follow-up observations revealing the systems to be stellar binaries. Further, we use these measurements to constrain the physical properties of the stellar components of the systems and their orbital

parameters. All the radial-velocity measurements used are listed in Table B.1.

2.1. TESS photometry

The TESS (Ricker et al. 2015) is a photometric space-based observatory operated by NASA, orbiting the Earth on a highly eccentric orbit with an orbital period of half a month. The satellite covers the sky in sectors of 24×96 degrees using wide-field cameras with 105 mm aperture, a focal ratio of $f/1.4$, and a spatial resolution of about half an arcminute. Each sector is covered continuously for two consecutive orbits with a brief interruption during the perigee used for data download. The survey was designed for the discovery of exoplanets via the transit method using a detector with a broad band pass around 6000–10 000 Å.

We used the MAST[1] archive to download the available short-cadence photometric time series as of September 2023. For our analysis, we used the LC_INIT time series of relative fluxes from the Data Validation Time Series product. These contain harmonics (of the satellite orbital period) removed, the sector edge detrended, normalized and stitched light curves from all available sectors as outlined in the TESS Science Data Products Description Document[2]. To model light curves it is necessary to add one to these values as the LC_INIT is shifted to an average normalized flux of zero. In cases where the LC_INIT was not yet available or where the light curve was visibly disturbed by the removal of harmonics (in the case of TOI-1788), we used PDC-SAP_FLUX fluxes from the relevant Light Curve Files, which we normalized by the mean value to obtain relative fluxes that can be appended to the previous data sets. We show one example sector of the photometric data used for each target in Fig. 1. The number of sectors in which the target was observed, N_{sectors}; primary eclipses contained within them, $N_{\text{prim.ecl.}}$; visibility of secondary eclipses; and other features in the light curves can be found in Table 1.

We checked the apertures used for light-curve extraction for field star contamination. Usually, we found no more than two sources with magnitude contrast $\Delta m < 7$. As an exception, TOI-1615 (a magnitude 9.7 target) has a denser background of tens of magnitude 17–18 stars within 100 arc-seconds, with one 13.5 mag star at 50 arcsec. The centroid motion of eclipses of all the targets is limited below one arcsecond, except for TOI-1153, which has a scatter of about 2 arcsec. The contribution from these distant sources is therefore negligible. For information about possible close-in companions identified through speckle imaging, we invite the reader to consult the corresponding subsections of Sect. 5.

Before fitting, we phased the light curves from all available sectors to make the data set more manageable. We used the linear ephemeris found in the headers of the Threshold Crossing Event files of the TESS Data Products and number of bins to retain the original cadence. In the case of TOI-1788, the light curve was dominated by variability, with a frequency different from the orbital frequency as can be seen in the bottom panel of Fig. 13. We used Period04 developed by Lenz & Breger (2005) to remove this contribution. First, we masked the eclipses and then computed the Fourier spectra to obtain the dominant frequency. Next, we fit the sine of this frequency and computed

---

[1] Barbara A. Mikulski Archive for Space Telescopes, https://mast.stsci.edu/portal/Mashup/Clients/Mast/Portal.html
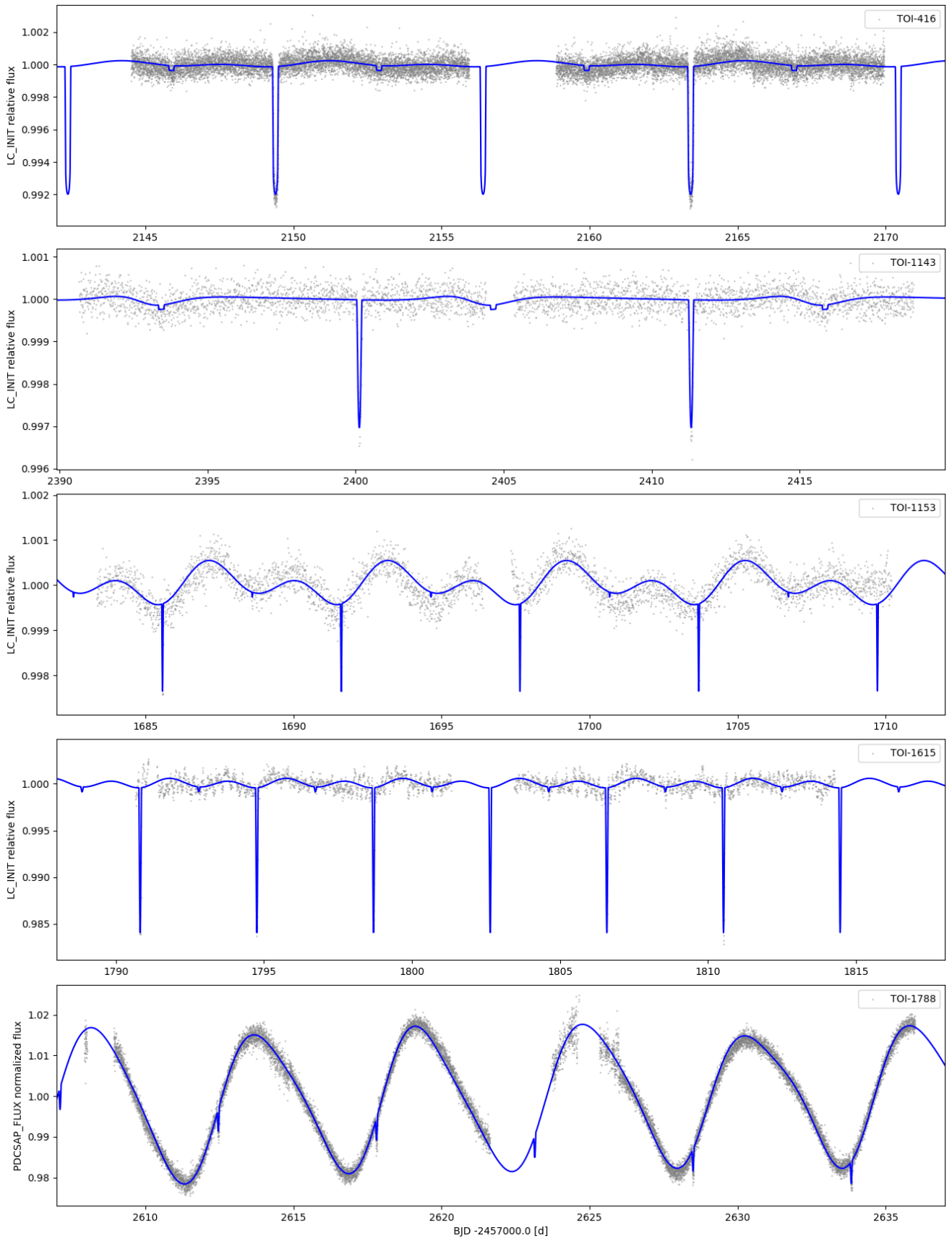[2] Available via https://archive.stsci.edu/missions-and-data/tess

Fig. 1. TESS light curves of the systems analyzed here. We only show one example sector per target. From top to bottom, TOI-416 (Sect. 31), TOI-1143 (Sect. 40), TOI-1153 (Sect. 14), TOI-1615 (Sect. 18), and TOI-1788 (Sect. 48). The blue line shows our binary fits with Doppler beaming included; in the case of TOI-1788, we also included model of rotational variability.

Table 1. Available TESS short-cadence photometry used in the analysis.

System	$N_{sectors}$	$N_{prim.ecl.}$	Sec. eclipse	Note
TOI-416	2	5	Weak	
TOI-1143	4	9	Weak	[a]
TOI-1153	7	30	Very week	[b]
TOI-1615	5	29	Weak	[c]
TOI-1788	1	4	No	[d]

Notes. [a]Shows an eccentric orbit. [b]asymmetric out of eclipse. [c]Small, δ-Sct-like variations at around 6 c/d. [d]Dominated by sinusoidal variation at $P = 5.55$ d.

spectra of the residuals. In this manner, we iteratively identified six main frequencies down to a relative flux amplitude of 0.0004, obtaining a fit of the following form:

$$F = F_0 + \sum A_i 2\pi(f_i t + \Phi_i), \tag{1}$$

where A_i is the amplitude of the contribution of frequency f_i with phase shift Φ_i.

2.2. Ondřejov Observatory spectroscopy

We used the Ondřejov Echelle Spectrograph (OES) installed on the Perek 2-m telescope operated by the Astronomical Institute of the Czech Academy of Sciences. OES is a fiber-fed échelle spectrograph with a resolving power of $R \approx 50\,000$ at 500 nm, covering the wavelength range of about 380–900 nm (Kabáth et al. 2020). The wavelength calibration was performed with ThAr lamp frames taken during the observing night. We observed the stars over a total of 57 nights. The typical exposure time was between 1800 and 3600 s. The signal-to-noise ratio (S/N) achieved ranged from 15 to 70.

The raw spectra were reduced with custom-prepared scripts using classical IRAF routines. The spectra were then corrected for instrumental shifts using telluric lines. The final product is a 1D merged spectrum from which the radial velocities were determined with IRAF's fxcor routine.

2.3. Tautenburg Observatory spectroscopy

The Tautenburg Coudé Echelle spectrograph (TCES) is installed on the 2 m Alfred-Jensch telescope operated by the Thüringer Landessternwarte Tautenburg. The instrument achieves a resolving power of $R = 67\,000$ with a slit-width of 1.2 arcsec. TCES has three cross-disperser grisms. For the observations, we used the so-called VIS grism, which covers the wavelength range from 460 to 730 nm. TCES is located in a temperature-stabilized room in the basement of the dome. The light from the star is injected into the spectrograph via a Coudé mirror train from the telescope. A temperature-stabilized I_2 vapor absorption cell placed in front of the slit provides a dense grid of absorption lines in the wavelength range from 500 to 640 nm. These iodine lines were used to determine the instrumental shift during the observations. Standard IRAF routines are used to subtract the bias, flat-field the spectra, remove the scattered light, extract the spectra, and wavelength-calibrate them. Radial velocity measurement was performed using Velocity and Instrument Profile Estimator (VIPER; Zechmeister et al. 2021).

2.4. FIES spectroscopy

We spectroscopically monitored TOI-416 with the FIbre-fed Echelle Spectrograph (FIES; Frandsen & Lindberg 1999; Telting et al. 2014) mounted at the 2.56 m Nordic Optical Telescope (NOT) at Roque de los Muchachos Observatory (La Palma, Spain). We acquired seven spectra using the FIES Med-Res fiber ($R = 45\,000$) at seven different epochs between January and February 2019, as part of the observing programs 58-024, 58-111, and 58-301 (PIs: Gandolfi, Hatzes, Deeg, respectively). We set the exposure time to 900–1500 s based on sky conditions and observing schedule constraints. Following Buchhave et al. (2010), we monitored the intra-exposure drift of the instrument by acquiring long-exposed ($T_{exp} \approx 60$–80 s) ThAr spectra immediately before and after each target observation. The FIES spectra were reduced using standard routines, as described in Gandolfi et al. (2013, 2015). Relative radial-velocity measurements were extracted using multi-order cross-correlations against the stellar spectrum with the highest S/N.

2.5. SONG spectroscopy

We also employed the 1m Hertzsprung SONG telescope (Grundahl et al. 2017) and its high-resolution échelle spectrograph located at Observatorio del Teide. The seven spectra obtained on seven consecutive nights starting January 28 have spectral resolutions of $\approx 80\,000$ and exposure times of 45 min. We used the procedures outlined by Grundahl et al. (2017) to extract the spectra. Bad pixels were removed, and the spectra were normalized. Subsequently, we used a template spectrum ($T_{eff} = 6300$ K, $\log g = 4.5$ [Fe/H] = 0) from the Phoenix library (Husser et al. 2013) to create cross-correlation functions (CCFs) from which we derived the RVs used in this work.

2.6. TRES spectroscopy

We used the Tillinghast Reflector Echelle Spectrograph (TRES) (Fűrész 2008) on the 1.5-m Tillinghast Reflector telescope at the Fred Lawrence Whipple Observatory (FLWO) in Arizona. TRES is a fiber-fed échelle spectrograph with a resolving power of $R \approx 44\,000$ operating in the 390 nm–910 nm wavelength range. Ten spectra were obtained from TOI-1143 during the period from November 2019 to February 2020. The exposure time ranged from 200 to 600 s, resulting in a S/N per resolution element of 16–43. The spectra were processed using a custom pipeline as described in Buchhave et al. (2010) using ThAr spectra obtained before and after observations as a calibration source. A multi-order spectral analysis was then performed. In short, each observation was cross-correlated against the strongest S/N spectrum, order-by-order, to obtain radial velocities.

2.7. WIYN imaging observations

We observed TOI-1143, TOI-1153, and TOI-1788 using the NN-EXPLORE Exoplanet Stellar Speckle Image (NESSI) (Scott et al. 2018) at the WIYN 3.5 m telescope on Kitt Peak, Arizona, USA. NESSI is a dual-channel instrument that obtains simultaneous speckle measurements in two filters using a pair of high-speed electron-multiplying CCDs. For each of our target stars, we obtained 9000 40 ms frames through filters with central wavelengths $\lambda_c = 562$ and 832 nm and band-pass widths of $\Delta\lambda = 44$ and 40 nm, respectively. The readout of each camera was restricted to a 256×256 pixel region, resulting in a 4.6×4.6 arcsec field of view. In addition to the TOI targets,

we obtained similar sets of 1000 speckle frames toward nearby single stars in order to calibrate the observational point spread function (PSF).

We reduced the speckle data using a pipeline described in Howell et al. (2011). Among the pipeline products is a reconstructed image of the field around each TOI in each filter. We identified any companion sources and measured contrast curves using these images. Although the reconstructed image covers a larger area, we have limited our contrast curves to an outer radius of 1.2 arcsec to avoid the decorrelation of speckle patterns at wider separations. Another pipeline product is a model fit to the power spectrum, which is derived from the Fourier transform of the mean of the autocorrelation function of each speckle frame. When a companion star is identified, a model fit to this power spectrum provides a measurement of the relative astrometry and photometry of the two sources. There was only one system with an identified companion, TOI-1143, which is shown in Fig. 4.

3. Spectral-energy-distribution fitting

To obtain the physical characteristics of the systems, we need some information about the primary stars. The measured radial-velocity amplitudes suggested the companions to be low-mass stars. The stellar parameters of the primaries were obtained by fitting their SEDs with ARIADNE (Vines & Jenkins 2022) – at first under the assumption that the flux contribution of the secondary is negligible. ARIADNE downloads available broad-band photometry[3], a subset of which is presented in Table 2, and fits it with the atmospheric models of Phoenix v2 (Husser et al. 2013), Kurucz (1993), Castelli et al. (2003), BT-Settl (Allard et al. 2012), BT-NextGen (Hauschildt et al. 1999; Allard et al. 2012), and BT-Cond (Allard et al. 2012). From these, the first four mentioned were used because BT-Settl, BT-NextGen, and BT-Cond are identical above $T > 4000$ K. To create model grids, atmospheric models corrected for distance, and interstellar absorption are convolved with the respective photometric spectral response functions to obtain model observed fluxes.

We fit for effective temperature (T_{eff}), radius (R), distance (D), surface gravity ($\log g$), metallicity ([Fe/H]), and line-of-sight extinction (A_V). For T_{eff} and $\log g$ priors, we used the TIC v8 catalog (Stassun et al. 2018) values. For [Fe/H], R, D, and A_V, we used the default ARIADNE priors. For [Fe/H], ARIADNE uses a Gaussian prior of $\mathcal{N}(-0.125, 0.234)$ based on data from the spectroscopic RAVE survey (Kunder et al. 2017)[4], D is drawn from the Bailer-Jones distance estimate from Gaia (Bailer-Jones et al. 2018), the prior for R is in the interval from 0.5 to $20\,R_\odot$, while the A_V prior is limited to the maximum line-of-sight extinction from the updated SFD Galactic dust map (Schlegel et al. 1998). Parameters obtained using ARIADNE under the one-star assumption are in Table 3. We stress that these parameters were obtained assuming that the stars are single. Nevertheless, we see good agreement between measured and modeled fluxes, so we used these values as good estimates of primary star properties within the binary systems. Later, we sub-

---

[3] ALL-WISE (Wright et al. 2010), APASS DR9 (Henden & Munari 2014), Pan-STARRS1 (Chambers et al. 2016), SDSS DR12 (Alam et al. 2015), 2MASS (Skrutskie et al. 2006), Tycho-2 (Høg et al. 2000), ASCC (Kharchenko 2001), GLIMPSE (Churchwell et al. 2009), GALEX (Bianchi et al. 2011), Strömgen Photometric Catalog (Paunzen 2015), Gaia DR2 (Gaia Collaboration 2016, 2018).

[4] Estimated metallicities from ARIADNE are comparable with those derived by spectral-reduction pipelines in ExoFOP. Moreover, metallicity only enters our model through pass-band luminosities via the atmospheric tables where the influence is known to be negligible.

Table 2. Astrometric and photometric data used for SED fitting.

TOI	416	1143	1153	1615	1788
α_{2000} [h m s]	03 15 25.1	12 10 09.3	12 10 46.0	23 24 41.9	10 40 55.0
δ_{2000} [° ′ ″]	−02 10 31	+77 21 08	+85 42 18	+77 37 37	+35 54 48
μ_α [mas/yr]	29.76(9)	−36.30(11)	−14.19(6)	12.59(5)	−48.38(8)
μ_δ [mas/yr]	−6.86(8)	4.19(8)	−2.27(5)	2.74(5)	−72.31(7)
D [pc]	132.0(8)	192.0(20)	147.1(6)	260.5(21)	191.5(24)
BT	9.423(21)	9.706(22)	9.250(18)	10.293(27)	11.602(68)
B	9.245(8)	9.599(36)	9.217(14)	10.388(92)	11.468(14)
BP	8.921(3)	9.262(3)	8.900(3)	10.064(3)	10.970(4)
VT	8.828(16)	9.138(17)	8.821(14)	10.008(27)	10.726(53)
y	8.770(20)	–	8.777(14)	10.09(11)	10.757(32)
V	8.929(4)	9.077(2)	8.773(2)	9.975(4)	10.602(17)
G	8.6604(28)	9.006(3)	8.701(3)	9.912(3)	10.637(3)
RP	8.2298(38)	8.581(4)	8.347(4)	9.639(4)	10.135(4)
T	8.282(6)	8.633(6)	8.405(6)	9.6871(6)	10.188(6)
J	7.776(24)	8.119(24)	7.965(29)	9.326(23)	9.628(24)
H	7.557(46)	7.874(20)	7.798(31)	9.229(27)	9.347(35)
K	7.473(21)	7.829(16)	7.738(16)	9.159(21)	9.239(23)
W1	7.383(36)	7.778(26)	7.706(30)	9.126(24)	9.160(23)
W2	7.458(20)	7.818(20)	7.733(23)	9.132(20)	9.188(20)

Table 3. Results of initial ARIADNE SED fitting ignoring the secondary components.

TOI	416	1143	1153	1615	1788
T_{eff} [K]	6238(70)	6242(65)	6691(80)	7120(80)	5742(34)
$\log g$	4.02(40)	4.37(30)	3.47(43)	4.11(30)	4.03(60)
[Fe/H]	−0.18(10)	−0.23(12)	−0.06(7)	−0.20(15)	0.02(6)
D [pc]	130.92(17)	187.30(12)	145.61(12)	254.8(12)	192.19(45)
R [$R_\odot$]	1.840(25)	2.234(25)	1.734(22)	1.533(22)	1.264(17)
A_V	0.09(4)	0.07(4)	0.09(6)	0.04(5)	0.03(1)

tracted model fluxes of the secondaries to refine the primary star parameters. These fits can be seen in Fig. A.1.

4. Light curve and radial-velocity fitting

To model the light curves, we used the PHOEBE software developed by Prša et al. (2016), which is an eclipsing binary modeling code with Python interface[5] using the PHOEBE 2.4 version. The astrophysical background of eclipsing binary stars and their modeling is described in detail in the book by Prša (2018). We generally followed the guide by Conroy et al. (2020) for the current version. We are, however, using PHOEBE mainly as a wrapper instead, using the ELLC forward model by Maxted (2016) describing the stars as ellipsoids and using Gauss-Legendre integration over projected ellipses to obtain measured fluxes. Passband fluxes and logarithmic limb-darkening coefficients were sourced from Phoenix atmosphere tables by Husser et al. (2013) to cover even the coolest companions.

In all cases, we used synchronously rotating stars in our models to describe the ellipsoidal shape of the stars. In case of small deviations from sphericity, the introduced error in stellar parameters is minimal. Bigger deviations are driven by more massive secondaries on close-in orbits, where synchronous rotation is expected. To illustrate the level of the possible errors introduced by this assumption, we estimated relative differences between the smallest and the biggest radius of curvature of tidally deformed stars. This would be the radii driving the shape of the light curve during eclipse for grazing eclipses with a tidal

---

[5] Freely available to download along with documentation and many examples at http://phoebe-project.org/

Table 4. Fits of light curves out of eclipse according to Equation (2).

System	$A \times 10^5$	$B \times 10^5$	$C \times 10^5$	$D \times 10^5$
TOI-416	-1.5 ± 6.1	10.9 ± 1.4	11.0 ± 2.0	2.3 ± 3.7
TOI-1153	10.7 ± 4.3	24.3 ± 2.5	30.7 ± 2.6	1.1 ± 2.8
TOI-1615	16.7 ± 5.3	25.6 ± 9.2	36.4 ± 9.7	3.5 ± 5.8
TOI-1788 [a]	-10.1 ± 1.6	0.1 ± 0.2	-7.5 ± 1.5	$\pm$

Notes. [a] Only one sector available; errors are from the least-squares fit and are thus grossly underestimated.

bulge aligned with the secondary and with a 90° lag. Using values from Pathania & Medupe (2012) for a mass ratio of $q = 0.4$ and fill-out factor of $F = 0.4$ (corresponds to $R_1/a \doteq 0.16$) as a worst case scenario for our systems, we see a difference of only 1.8%. This upper estimate of the introduced error is of the same magnitude as the uncertainty in the primary radii themselves. In case of systems with precisely determined parameters – TOI-416 and TOI-1143 – this estimate is closer to the case with $q = 0.1$, $F = 0.2$, leading to a difference of only 0.23%. To obtain the proper posterior distributions of model parameters, we used the EMCEE Markov chain Monte Carlo sampler by Foreman-Mackey et al. (2013).

4.1. Preliminary step

In some of our systems, the effect of Doppler beaming and boosting is clearly visible (see Zucker et al. 2007 for the description of Doppler beaming in a binary star context). The current version of PHOEBE does not support this effect; therefore, we proceeded to fit the light curves outside the eclipses by the following function:

$$F(\Phi) = F_0 - A\cos(2\pi\Phi) + B\sin(2\pi\Phi) - C\cos(4\pi\phi) + D\sin(a\pi\Phi),$$
(2)

which describes the total flux F as a function of an orbital phase Φ. The sum consists of a constant term F_0, a reflection term with amplitude A, a relativistic beaming and boosting term of amplitude B and geometric ellipsoidal variation of amplitude C. The coefficient D should be zero and was added as a further mean to estimate errors of the other parameters. This description was shown by Faigler & Mazeh (2011) as a good means of describing out-of-eclipse variability in close binaries. We note that the boosting term is proportional to the radial velocity, so the above description is valid for circular orbits only. The constant of proportionality can, in principle, be derived from the spectra of the star and the detector pass band. For now, we use it as a free parameter instead.

We performed separate fits for every sector and then computed averaged values of the coefficients presented in Table 4. We omit the F_0 term from the table. It is only a shift of a few 10^{-5} in normalization, given by the difference between the flux used to normalize the light curve initially and the mean flux of the stars in the ellipsoidal model. The mean normalized flux of the system is a free parameter in our subsequent model. Signs in Equation (2) were chosen so that the respective coefficients, A, B, and C, would be positive. Parameter errors of the least-squares fits were around $(0.5-1.5) \times 10^{-5}$, while the scatter of the values between sectors was larger. We attribute this discrepancy to the instrumental systematics in the light curves and to the detrending algorithm used by the PDC-SAP pipeline. The values of D are consistent with zero. We see that in the case of TOI-1788,

the value of A and C is quite negative – this is a consequence of the smoothing performed for this system to remove rotational variability, and thus we cannot expect the residual out-of-eclipse variability to be of an astrophysical nature. As a result, for TOI-1788 we only model the primary eclipse. For the other systems, we subtracted the contribution of beaming and boosting from the data such that PHOEPE can model the other two effects directly. We excluded TOI-1143 from this quick analysis because of its eccentric orbit.

4.2. Main step in PHOEBE

As the next step, we jointly modeled the radial velocities from all available instruments using the period derived from the eclipses. We used the following set of variables as the parameters to be estimated: the projected semi-major axis of the primary around the barycenter ($a_1 \sin i$), the eccentricity projections ($e\sin\omega$, $e\cos\omega$), and the systemic velocities (γ_i) of each data set and their respective factors of error underestimation (σ_i). From this, the primary's radial-velocity semi-amplitude (K_1) and the mass function ($f(M)$) can be computed using the period of the system (P) and Newton's gravitational constant (G) as follows:

$$K_1 = \frac{2\pi}{P}\frac{a_1\sin i}{\sqrt{1-e^2}}, \quad f(M) = \frac{4\pi^2}{P^2}\frac{(a_1\sin i)^3}{G}.$$
(3)

Next, we fit the light curves solving for the ratio of stellar radii (R_2/R_1), inclination (i), ratio (($R_1 + R_2$)/a) of the sum of stellar radii over the semi-major axis, primary pass-band luminosity ($L_{pb,1}$), and ratio of secondary and primary effective temperature (T_2/T_1) as well as the projection of $e\cos i$ if a secondary eclipse was present. Here, we fixed the primary radius (R_1) and temperature (T_1) according to the ARIADNE fits, and $a_1 \sin i$ and eccentricity projections according to the radial-velocity fit. We used initial values suggested for main-sequence stars by Pecaut & Mamajek (2013) using the TESS Input Catalogue parameters as a guide for the primary, and we manually adjusted the inclination to match the depth of the eclipses. From these values, the semi-major axis of the binary and mass ratio can be computed as

$$a = R_1\frac{1 + \left(\frac{R_2}{R_1}\right)}{\left(\frac{R_1+R_2}{a}\right)}, \quad q = \frac{(a_1\sin i)}{a\cdot\sin i - (a_1\sin i)},$$
(4)

which yields the masses of the components using the third Kepler's law.

As a final step, we refined the parameters by running the radial velocity and light-curve fit together. We also attempted to fit for the albedo of the secondary (A_2) and the gravity brightening coefficient of the primary (β_1), but we did not achieve conclusive results. We note that the simultaneous solution of radial velocities and light curves often converged to incorrect values of eccentricity projection, $e\sin\omega$ and $a_1\sin i$, with only small visual differences in light curves but unsatisfactory fits in radial velocities. We believe this is the consequence of light-curve domination of the solution given by the order-of-magnitude difference in the number of photometric and RV points used in the fit.

4.3. Correction for binarity

After successfully fitting the combined radial-velocity and photometry data with PHOEBE, we computed magnitude corrections

from fractional light in the photometric channels to obtain magnitudes of the primary star alone. We subsequently used these to perform new ARIADNE SED fits. If the results were similar to the previous values, we performed the following simple corrections for the parameters. Fixing the previously fit T_2/T_1, R_2/R_1 and $(R_1 + R_2)/a$, we obtain corrected values for secondary star temperature and radius and orbital semi-major axis as a simple scaling:

$$T_2 = \frac{T_1}{T_1^{\text{old}}} T_2^{\text{old}}, \quad R_2 = \frac{R_1}{R_1^{\text{old}}} R_2^{\text{old}}, \quad a = \frac{R_1}{R_1^{\text{old}}} a^{\text{old}}. \quad (5)$$

Radial-velocity-dependent parameters are fixed, so for the mass ratio we have

$$\frac{aq}{1+q} = a_1 = \text{const.} \quad \rightarrow \quad q = \frac{a^{\text{old}}}{a} \frac{q^{\text{old}}}{1 + q \frac{a - a^{\text{old}}}{a}} \approx \frac{R_1^{\text{old}}}{R_1} q^{\text{old}}. \quad (6)$$

For the masses, we thus have the following correction from Kepler's third law:

$$M_1 = \left(\frac{R_1}{R_1^{\text{old}}}\right)^3 M_1^{\text{old}}, \quad M_2 = \left(\frac{R_1}{R_1^{\text{old}}}\right)^2 M_2^{\text{old}}. \quad (7)$$

These equations also serve to estimate the uncertainty of these parameters due to the uncertainty of the primary radius, which was fixed during the PHOEBE run.

For cases where the binarity corrections for R_1, T_1 were larger than the uncertainties on the values themselves, we made a new PHOEBE photometry model to accommodate this. The main reason is that the temperature change can influence coefficients of limb darkening and pass-band luminosities, which can change the shape and depth of the eclipse in the forward model necessitating a change in inclination i and ratios R_2/R_1 and $(R_1 + R_2)/a$.

5. Results

5.1. TOI-416

The seventh-magnitude star HD 20267 (BD−02 583, TIC 49899799) in the northern part of Eridanus was identified as an exoplanetary candidate, TOI-416, in January 2019. It was also recovered in an eclipsing binary study by Prša et al. (2022) searching for eclipsing binaries in TESS. The star shows total primary eclipses with secondary eclipses also visible on a nearly circular seven-day orbit, as can be seen in Fig. 2. There is no significant contaminant in the surrounding field. The Gaia astrometric solution yields a renormalized unit weight error (RUWE) of 1.12, and there are no detected companions within 0.2″ (which is about 30 au at the distance of the main source) according to speckle imaging at SOAR by A. Tokovinin available via ExoFOP archive. In our analysis, we used our 12 radial-velocity measurements from the Ondřejov Observatory, seven measurements from the SONG node on the island of Tenerife by S. Albrecht via the ExoFOP archive, and seven measurements by FIES. In Fig. 3, we can see a circular orbit with an amplitude of about 11 km/s, signalling a very low-mass stellar companion.

Our SED fit, corrected for the light of the secondary, yielded a temperature of $T_1 = 6330(60)$ K, radius of $R_1 = 1.82(2)$ $R_\odot$, surface gravity of $\log g = 4.02(5)$, metallicity of [Fe/H] = $-0.18(10)$, and an isochrone mass of $M_1 = 1.31(7)$ $M_\odot$. We note that these values are comparable to Gaia spectroscopy and spectroscopy by A. Bieryla by TRES at FLWO, except for the temperature. Our temperature estimate is about 300 K higher
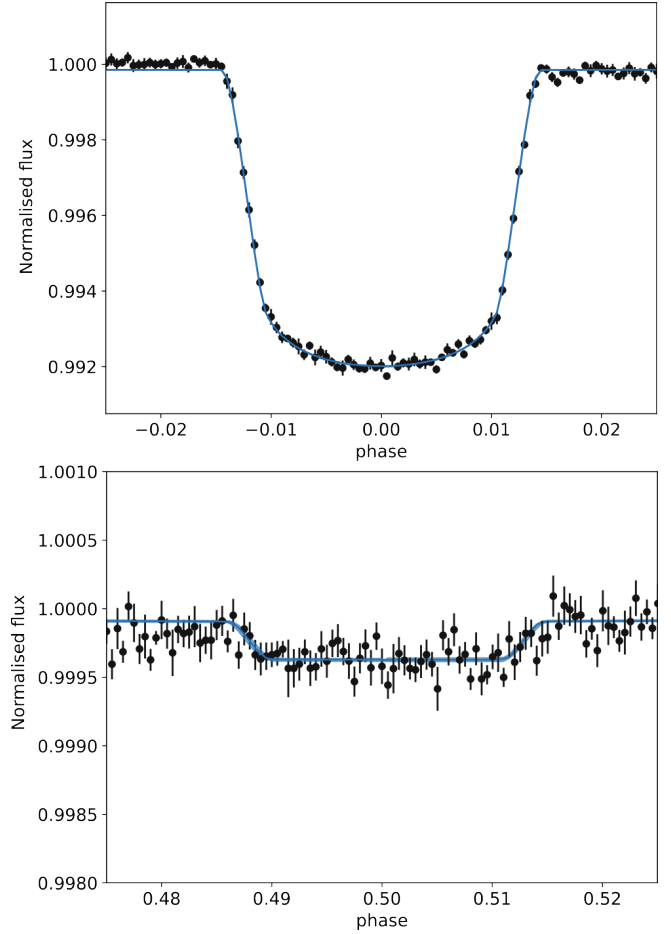

Fig. 2. Light curve of TOI-416. We can see the total primary eclipse in the upper panel and shallow secondary eclipse in the bottom panel.

than both TRES and Gaia. We also note that the projected rotational speed of the primary from the TRES spectral analysis of $v \sin i = 10.3(5)$ km/s is lower than the expected value for synchronous rotation $v_{\text{syn}} = 13.1(2)$ km/s.

The resulting parameters from our fit can be seen in Table 5. Posteriors of the fit parameters were Gaussian, containing small covariances with the exception of i and $(R_1 + R_2)/a$, which are tightly bound in anticorrelation by the duration of the eclipse. We also tried to fit for the bolometric (Bond) albedo of the secondary (A_2) and bolometric gravity darkening coefficient of the primary (β_1), without success. We thus kept them at suggested values: $\beta_1 = \beta_2 = 0.32$ and $A_1 = A_2 = 0.6$. We can see that the orbit of the star is indistinguishable from a circular one. The binary consists of a 1.36(7) $M_\odot$ primary (in good agreement with the ARIADNE fit) evolving from the main sequence and a secondary with a mass of just 0.131(8) $M_\odot$ on the main sequence of spectral class M5V. Our ARIADNE-MIST estimate for the age of the primary and thus the age of the system of 2.9(5) Gyr provides enough time for the circularization of the orbit. The slow rotation speed of the primary can be explained by the evolutionary expansion of the envelope of the star, which slows down the rotation from the previous synchronized state.

5.2. TOI-1143

The northern star of ninth magnitude, BD+78 407 (TIC 160268701), was flagged as a possible exoplanetary candidate
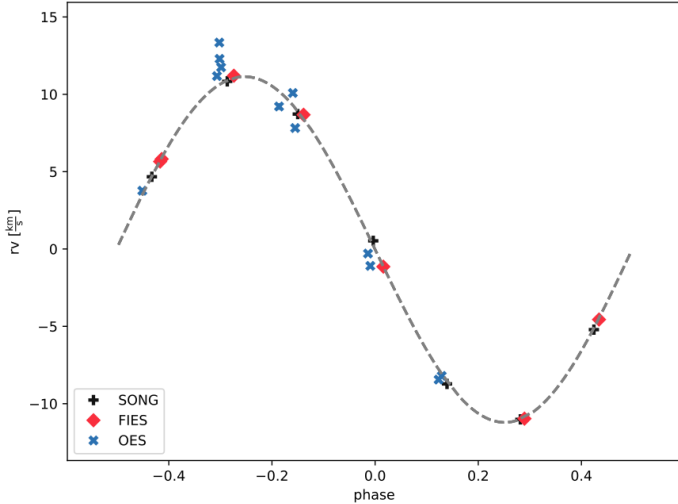
Fig. 3. Radial velocity curve of TOI-416 obtained by OES, SONG, and FIES corrected for the instrumental zero points with the best-fit solution shows a circular orbit of the system. Errors of the data points are smaller than the markers.

Fig. 4. Contrast curves for TOI-1143 showing the detection limit of NESSI speckle imaging in the 562 nm (blue curve) and 832 nm filters (red curve). The star symbol indicates the separation and contrast of the detected companion. A reconstructed image for each filter is shown in the upper right, with TOI-1143 in the center of the field. The companion appears as a pair of close-by sources lying roughly north and south of TOI-1143. The double image is due to an ambiguity in the image reconstruction. These images are oriented with north at the top and east to the left.

by TESS in August 2019. The light curve shows an 11.2-day eccentric orbit with a shallow secondary minimum around phase 0.4. A search of the Gaia catalog reveals no close stars significantly contaminating the light of the target. However, the star shows quite a big astrometric excess error with RUWE = 5.05, hinting at a possible close companion. This star was resolved by NESSI at a separation of 0.12″ and a magnitude difference of $\Delta m = 2.07(10)$ in both V and I filters, as can be seen in Fig. 4. The position angle of the companion star in this instance is ambiguous by 180 deg, meaning its true position angle could be either 4° or 184°. We adopted a third-light ratio of 12.9(10)% in the photometric fit, and we corrected the radius of the star from ARIADNE by the corresponding amount. The nature of this star is discussed later. We had 40 radial-velocity measurements from Ondřejov and ten from TRES at our disposal. To obtain a more precise linear ephemeris, we also used long cadence TESS observations from Sector 14 on top of short cadence sectors 47, 48, 53, and 60.

After the correction for the binary companion and the contaminant we obtained a temperature $T_1 = 6300(50)$ K, radius $R_1 = 2.069(18)$ R$_\odot$, $\log g = 3.85(5)$ and metallicity [Fe/H] = $-0.21(10)$. This is slightly hotter than the spectroscopic fit by L. A. Buchhave using NOT-FIES data with $T = 6100(50)$ K, while the surface gravity and metallicity are in good agreement. They also reported a value of projected rotational velocity of $v \sin i = 11.1(5)$ km/s, implying a rotational period of up to $P_{rot} \doteq 9.4$ day, which is shorter than the orbital period. However, due to the eccentricity of the orbit, the expected pseudo-synchronized rotational period of the primary (Hut 1981) is about $P_{rot}^{ps} = 7.5$ day, which is greater than the observed one.

Our photometric fit in Fig. 5 models the observed light curve nicely using the suggested gravity-brightening-coefficient values and albedos of the stars. The posteriors have only small covariances, with the exception of i and $(R_1 + R_2)/a$. The radial-velocity curve in Fig. 6 reveals the eccentricity of the orbit and low mass of the stellar companion. Furthermore, two data points near the primary eclipse are outlying suggesting presence of the Rossiter-MacLauglin effect. However, the expected amplitude is well under 100 m/s, and latter point happens after the eclipse is finished. We therefore discarded these points in our analysis. The
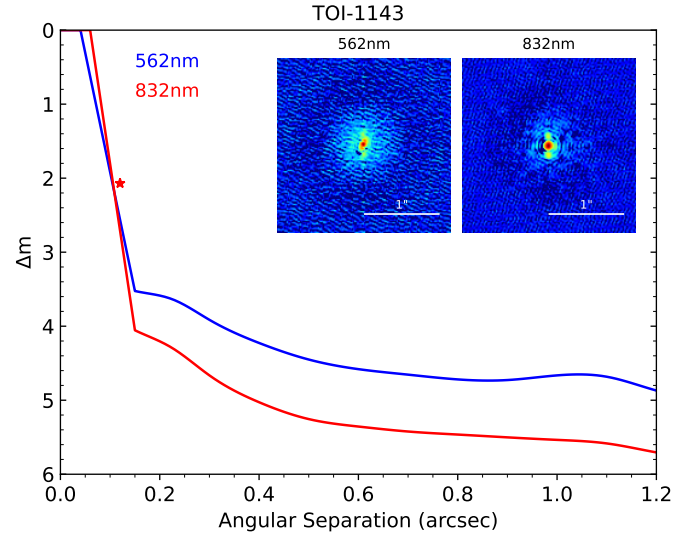
parameters of the system can be found in Table 5. The primary star is an evolved sub-giant star. Pecaut & Mamajek (2013) suggested a temperature about 700 K hotter and radius 23% smaller for a main-sequence star of the same mass. The secondary has a mass of $M_2 = 0.118(5)$ M$_\odot$, which is consistent with an M5.5 dwarf, although our temperature estimate of $T_2 = 3210(60)$ K is about 300 K too high for a main-sequence star. This can be caused by an underestimation of the secondary albedo. However, the estimated temperature is for the irradiated face of the star just after periastron passage. It can be higher than expected in case the rotation of the secondary is synchronous and heat transfer not very effective.

Finally, we discus the nature of the companion detected in the imaging. The magnitude difference of 2.07 mag with respect to the primary in both V and I filters would suggest a star of the same temperature behind the binary system. In spite of that, the field surrounding TOI-1143 is quite sparse, containing only about 50 sources brighter than the imaged companion inside a one degree radius. If we consider a disk with a radius of 0.12″, we would expect just $1:10^{-7}$ stars inside it at this stellar density. Therefore, it is highly unlikely that the imaged companion is just a star in the foreground or background. If we consider the errors of the contrast measurements $\Delta I = 0.1$ and $\Delta V = 0.15$, we obtain an error in the colour of $\Delta(V - I) = 0.18$. According to Pecaut & Mamajek (2013), for stars at the same distance (if we correct for the difference in radius of our primary and a main-sequence star of the same temperature), the contrast of 2.07 in the I band would suggest a main-sequence star with a temperature around 5550 K. Here, the companion would be redder by 0.18 in $V - I$, which is not strongly ruled out by the imaging colour. We thus conclude that the imaged star is a bound companion in the system.

The angular separation of the companion translates to a tangential separation of 23 au and minimal possible orbital period of ≈25 y, assuming the currently observed separation is equal to
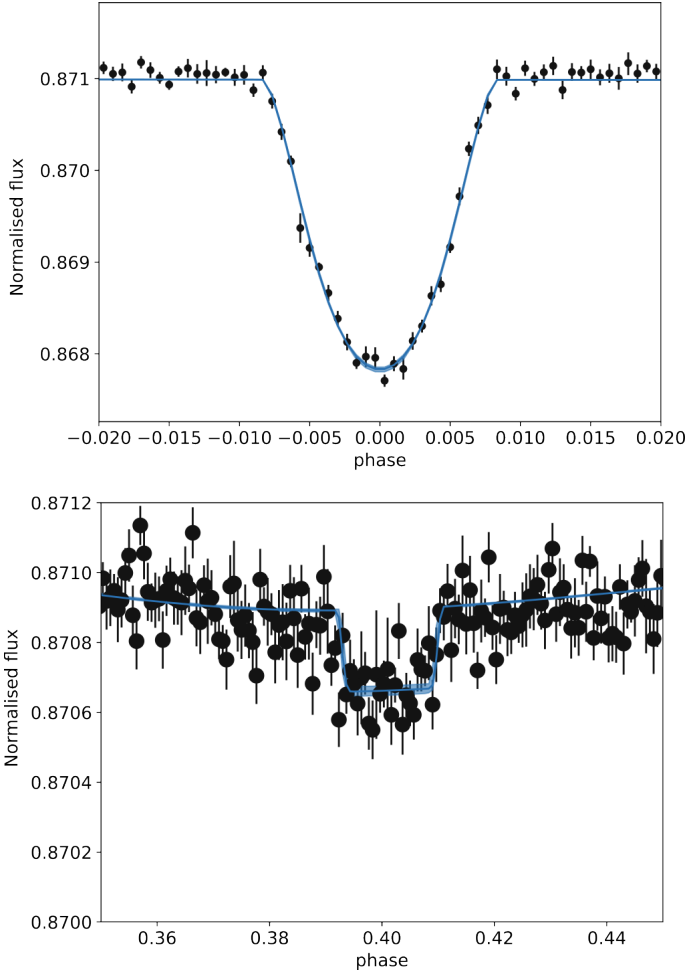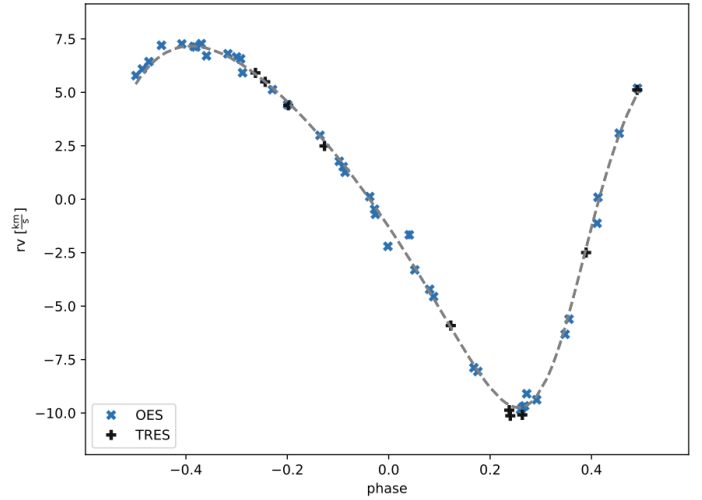
Fig. 6. Radial velocity curve of TOI-1143 obtained by OES and TRES corrected for instrumental zero point with our best-fit solution on an eccentric orbit. Errors of the data points are smaller than the markers.

Fig. 5. Light curve of TOI-1143. We can see the total primary eclipse in the top panel and shallow secondary eclipse offset from the phase 0.5 by its eccentric orbit in the bottom panel.

twice the semi-major axis as an extreme scenario. This changes to ≈ 100 y for $a = 23$ au equal to the tangential separation and ≈ 200 y for $a = 33$ au for a circular orbit if the companion is seen at elongation and halfway between elongation and conjunction, respectively. This would imply a variability in systemic velocity of the central binary up to $\approx 5-10$ km/s in the edge-on case and respective changes in eclipse timing of amplitude of tens of minutes up to an hour on a decadal to centennial timescale. We checked the residuals of the Ondřejov radial-velocity measurements spanning ≈ 300 d by fitting a quadratic polynomial: $f(x) = a+bx+cx^2$. However, the constant comparison fit resulted in χ^2_{NDF} smaller by about 5% preferring the non-detection of the companion. We placed 3σ upper limits on the coefficients $b < 0.0021$ km/s/d and $c < 0.000033$ km/s/d^2. Assuming a circular orbit of period P_3, one can derive the relation for the observed reflex motion of the central binary:

$$K_3 = b^2 \left(\frac{P_3}{2\pi}\right)^2 + 4c^2 \left(\frac{P_3}{2\pi}\right)^4. \tag{8}$$

Using our limits on b,c and the minimal conceivable period $P_3 = 25$ y, we obtain the 3σ limit $K_3 < 140$ km/s. Our radial-velocity observations are thus unable to place any reasonable limit on the orbit of the third body in the TOI-1143 system.

For completeness, we also considered the option that the low-mass companion is orbiting the imaged companion. Assuming the third light $l_3 = 87\%$ and primary star radius $R_1 = $

0.93 R$_\odot$, we obtained a radius for the secondary $R_2 = 0.16(1)$ R$_\odot$ and the sum of the masses of the components, $M_1 + M_2 = 0.53(5)$ M$_\odot$. To explain the ellipsoidal variation, it is further necessary to use high-mass ratios around 1.7, leaving us with a primary star with a mass of just $M_2 = 0.20$ M$_\odot$, which is clearly outside of range for both stars and white dwarfs. Therefore, we rule out this possibility.

5.3. TOI-1153

The ninth-magnitude star HD 106018 (BD+86 177, TIC154840461) in the northern part of Camelopardalis was recognized as a possible transiting exoplanetary candidate by TESS in September 2019. It was also recovered from the same data in an eclipsing binary study by Prša et al. (2022). The light curve shown in Fig. 7 with a 6.0-day period features significant out-of-eclipse variations and a V-shaped primary eclipse, suggesting a binary star with grazing eclipses and ellipsoidal variability. The detection of an extremely shallow secondary eclipse in the binned data is tentative. There are no close companions detected in imaging with NESSI@WIYN by Mark Everett (with a sensitivity level of 3^m down to $0.12''$). It has a low TIC-contamination ratio of only 0.00035 and a Gaia astrometric error of RUWE = 1.057, further suggesting an uncontaminated binary system. We used 29 radial-velocity measurements by the Tautenburg Observatory, showing a circular orbit with a semi-amplitude of about 45 km/s, shown together with our fit in Fig. 8.

The primary star has a temperature of $T_1 = 7000(130)$ K and a radius of $R_1 = 1.669(22)$ R$_\odot$ after correction for the secondary. For comparison, the spectral fitting done by L. A. Buchhave using NOT-FIES yielded a temperature of $T_1 = 6700(50)$ K, $\log g = 4.14(10)$, metallicity of [Fe/H] = $-0.04(8)$ and high rotational speed of $v = 10.9(5)$ km/s implying a rotational period of about $P_{\mathrm{rot}} = 7.7(2)$ days; this is slightly higher than the orbital period of $P = 6.0$ d.

The determination of the parameters of the stars is complicated by the grazing nature of the primary eclipse, creating a degeneracy between the inclination and the ratio of $(R_1 + R_2)/a$ and R_2/R_1, given the fact that the eclipse is basically described only by depth and duration. We tried to use the out-of-eclipse
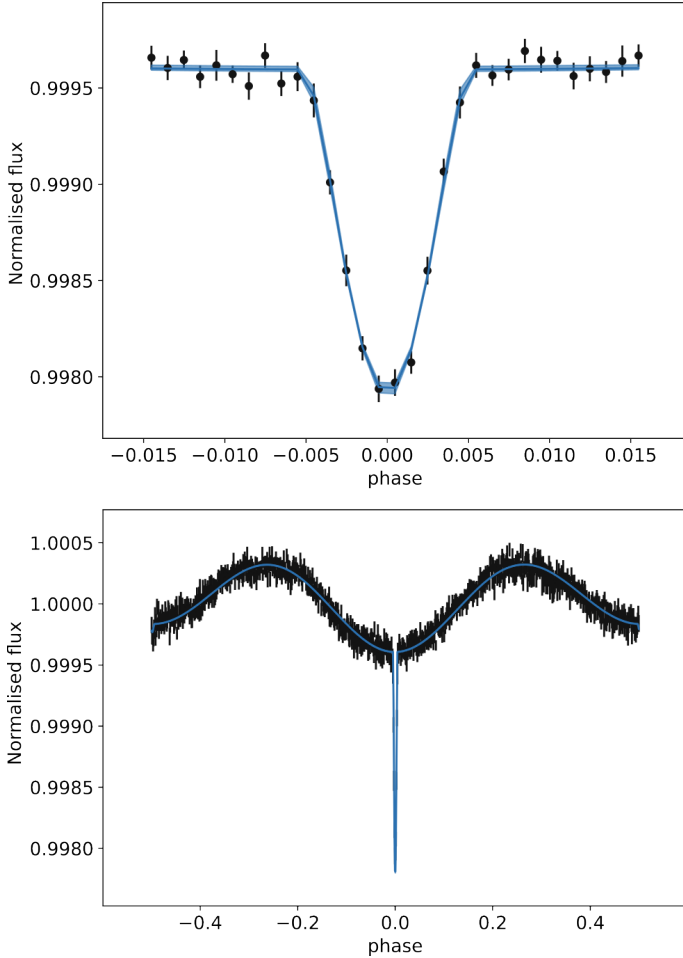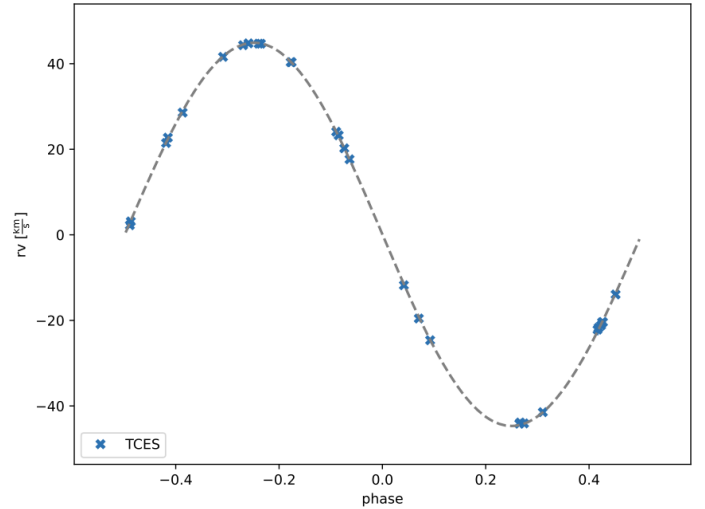
Fig. 8. Radial velocity curve of TOI-1153 obtained by TCES after zero-point correction with our best-fit model showing a circular orbit. Errors of the data points are smaller than the markers.

Fig. 7. Light curve of TOI-1153. The primary eclipse is shown in the top panel, and the full phase curve showing significant ellipsoidal variation in the bottom panel. We do not detect conclusive evidence of secondary eclipses.

5.4. TOI-1615

The ten-magnitude star BD+76 916 (TIC 317507345) in the constellation of Cepheus was identified as an exoplanetary candidate, TOI-1615, by the TESS survey in December 2019. It was also recovered from the same data in an eclipsing binary study by Prša et al. (2022). With a period of 3.94 days, the light curve shows a V-shaped primary eclipse and a shallow secondary visible in the binned data from all available sectors. There is also a quasi-periodic variation with a frequency of about six cycles per day, which we attribute to δ-Sct (DSCT) variability of the primary star. This variation is eliminated from the light curve by binning the photometric data phased with the orbital period. There is no imaging available in the ExoFOP database; however, there are a few faint stars in the surroundings with a TESS contamination ratio of about 0.014. The star has a moderately high astrometric solution error of RUWE = 1.446, which is higher than what is typical for an isolated target, but still not so excessive that it can unequivocally indicate a companion. Thus, we consider the binary system as alone. We have 17 radial-velocity measurements from Ondřejov at our disposal plotted in Fig. 10.

The temperature of the primary star was estimated by ARIADNE as T_1 = 7380(80) K after the binary correction with a radius of R_1 = 1.498(15) R$_\odot$. The spectroscopic work by A. Bieryla at TRES@FLWO in the ExoFOP archive shows the temperatures of 7212(73) K and 6935(88) K for the two spectra obtained, gravity of $\log g$ = 4.2(1), metallicity of [Fe/H] = 0.1(1), and $v \sin i$ = 12(1) km/s. In the case of parallel rotational and orbital axes, this yields a rotation period around P_{rot} = 6.3 d, which is clearly slower than the orbital period P = 3.94 d.

Our combined RV+photometric model reveals an almost circular orbit with an orbital velocity semi-amplitude of K_1 = 40.90(17) km/s. However, there is some degeneracy in the i, R_2/R_1, $(R_1 + R_2)/a$ space due to the V-shaped primary and secondary eclipses presented in Fig. 9. We thus provide two resulting sets of parameters in Table 5 – with this degeneracy and the additional use of primary mass from isochrone fit in italics. We can see that the masses of the stars are only determined with 10% accuracy without this aid. The primary star is of spectral class A9 judging by the temperature, but with a diameter of only 86% of the expected value for a main-sequence star (Pecaut & Mamajek

variability, which is evident in the light curve in Fig. 7, to adress this issue. For a star with a temperature from 6700−7000 K and $\log g$ = 3.5−4.5, the gravity-darkening coefficient should be around β_1 = 0.26(2) according to Claret (2003). From the amplitude of the ellipsoidal variability C = 8.71(5) × 10^{-5} and the primary radius, we can derive the semi-major axis of the binary a = 18.3(3) R$_\odot$. Alternatively, we can use the mass estimate from isochrone fitting in ARIADNE, arriving at a = 18.35(11) R$_\odot$, which is consistent with the previous value. We present our results under these assumptions separately in Table 5.

Information about the secondary is very limited. We only obtained masses of M_2 = 0.66(3) M$_\odot$ or M_2 = 0.667(13) M$_\odot$, with a reasonable precision level breaking the degeneracy using the ellipsoidal variation and isochrone fit for the primary, respectively. For the radius and temperature, we can only make crude estimations of 0.35 < R_2 < 0.8 from the shape of the primary eclipse and T_2 = 3050(350) K from the depth of the very shallow secondary eclipse. We note that the temperature estimate is highly uncertain – the value above does not consider possible changes in the secondary eclipse depth due to changes in eccentricity. For a star of the spectral class K6.5V, Pecaut & Mamajek (2013) gave a mass of M = 0.66(2) M$_\odot$ and radius of R = 0.65(1) R$_\odot$, which fall into our range and temperature of T = 4200(50) K, which is significantly higher than our estimate.

Table 5. Derived parameters of the orbit and component stars from SED, RV, and photometry, with the additional use of MIST isochrone fit for the primary in italics.

Target	TOI-416	TOI-1143	TOI-1153	TOI-1615	TOI-1788
Orbital period P [d]	7.011396(3)	11.207189(17)	6.036078(3)	3.9401793(6)	5.343604(6)
Superior conjunction t_0 [d]	1413.19585(17)	2400.1247(6)	1685.5773(3)	1790.82286(13)	2612.4629(8)
(BJD − 2457000)					
Semi-major axis a [$R_\odot$]	17.6(3)	24.8(3)	18.3(3)/*18.35(11)*	14.1(4)/*13.44(9)*	13.7(20)/*13.4(5)*
Eccentricity e	<0.010	0.285(4)	0.0032(11)	0.011(4)	0.070(7)
Argument of periastron ω [°]	–	238.0(5)	13(31)	68(12)	33(11)
Inclination i [°]	86.12(13)	86.24(5)	83.1(7)	83.6(5)	84(2)
RV semi-amplitude K_1 [km/s]	11.327(8)	8.44(7)	44.74(8)	40.90(17)	19.6(4)
Mass function $f(M)$ [$M_\odot$]	0.001056(3)	0.000 623(16)	0.0560(3)	0.02792(34)	0.00412(24)
Mass ratio q	0.0976(22)	0.0783(12)	0.415(6)/*0.415(3)*	0.294(13)/*0.313(4)*	0.18(3)*0.183(8)*
TESS third light l_3 [%]	–	12.9(10)	–	–	–
Primary component					
Volumetric radius R_1 [$R_\odot$]	1.82(2)	2.07(3)	1.67(2)	1.498(15)	1.26(2)
Mass M_1 [$M_\odot$]	1.36(7)	1.51(7)	1.60(6)/*1.61(3)*	1.87(16)/*1.60(3)*	1.1(5)/*0.96(7)*
Effective temperature T_1 [K]	6330(60)	6300(50)	7000(130)	7380(80)	5760(30)
Surface gravity $\log_{10}[g_1]_{cgs}$	4.05(3)	3.99(2)	4.20(2)/*4.20(1)*	4.36(4)/*4.29(1)*	4.3(3)/*4.22(4)*
Mean density $\log_{10}[\rho_1]_{cgs}$	−0.49(3)	−0.62(2)	−0.31(3)/*−0.31(2)*	-0.11(5)/*−0.17(2)*	−0.1(3)/*−0.17(4)*
Secondary component					
Volumetric radius R_2 [$R_\odot$]	0.157(2)	0.142(3)	$0.35 < x < 0.8$	0.32(7)	>0.09
Mass M_2 [$M_\odot$]	0.132(8)	0.118(5)	0.66(3)/*0.667(13)*	0.55(5)/*0.501(14)*	0.19(10)/*0.178(15)*
Effective temperature T_2 [K]	3010(40)	3210(60)	3350(550)	3480(80)	–
Surface gravity $\log_{10}[g_2]_{cgs}$	5.17(3)	5.21(3)	–	5.2(2)/*5.1(2)*	–
Mean density $\log_{10}[\rho_2]_{cgs}$	1.68(3)	1.76(3)	–	1.3(4)/*1.3(4)*	–

2013). Both of the mass estimates are in accordance with the hotter case. If we took the TRES temperatures and our radius, the star would still be too small in radius to be a main-sequence star. The secondary is an early M dwarf with estimates of M1, M2.5, and M3 from mass, temperature, and radius, respectively. This system is thus not described well as a pair of main-sequence stars. There are two possible explanations:

– our ARIADNE fit is "too hot"; a colder star could allow a larger primary radius in the SED and thus a bigger secondary.
– the fit is right, but the stars are not evolving as well-separated main-sequence stars.

After the binary model removal from the light curve, we identified the main pulsation frequency of $f_0 = 6.303\,\mathrm{d}^{-1}$ and amplitude 0.00066 relatively to the light m of both stars, with S/N of 9.2. There are also secondary frequencies of $f_1 = 6.376\,\mathrm{d}^{-1}$ and $f_2 = 6.197\,\mathrm{d}^{-1}$ present with about half the amplitude of f_0. This variability presented in Fig. 11 combined with the derived effective temperature clearly shows that the primary of TOI-1615 is a multi-mode DSCT.

It is worth noting that we can neglect the effect of pulsations on the radial-velocity values and the estimation of stellar parameters from the binary model. The ratio of radial velocities and visual amplitudes of DSCT stars is between 50 and $125\,\mathrm{km}^{-1}\,\mathrm{mag}^{-1}$ (Breger et al. 1976). The amplitude of pulsations is about 3 mmag (see Fig. 11), which translates to an expected amplitude of $0.15-0.375\,\mathrm{km/s}$. In addition, the exposure time of the individual exposures was one hour (1/4 of the pulsation cycle), which decreases the observable radial-velocity amplitude of the pulsations. These values are comparable to the uncertainties of our radial-velocity observations (Table B.1). Finally, the observations were taken randomly with respect to the pulsation cycle, so the effect of pulsations averages out.

5.5. TOI-1788

In Leo Minor, there is an eleventh magnitude star TYC 2518-812-1 (TIC 450327768) that was identified as TESS exoplanetary candidate TOI-1788 in March 2020. It was also identified as a spectroscopic binary by Gaia Collaboration (2023). There is no companion present in an imaging study using NESSI@WIYN by Mark Everett (with a sensitivity of 3.5^{m} down to 0.15″). It has a renormalized astrometric excess error of RUWE = 1.028 in Gaia and a negligible TESS contamination ratio, suggesting a lone system. The TESS light curve shows four primary eclipses with a period of $P = 5.344\,\mathrm{d}$ and no secondary eclipses visible; there are also sinusoidal changes in total light, with a period of $P = 5.549\,\mathrm{d}$ and an amplitude up to 0.02 in normalized flux in the only available short cadence sector from February 2022. We detrended this variability prior to the binary parameter fit as described in Sect. 2.1. We discuss its nature later. We have at our disposal 13 radial-velocity measurements from the Ondřejov Observatory and 18 from Tautenburg Observatory, which are displayed in Fig. 12. There is also one long cadence TESS sector (Sect. 21) with four additional eclipses available; however, it contains only three or four points per eclipse. Also notable is the partial observation of the eclipse from the ground on January 21, 2022 UT with the MuSCAT2 multicolor imager (Narita et al. 2019) installed on the 1.5 m Telescopio Carlos Sánchez (TCS) at the Teide Observatory, Spain, with the eclipse center at $T_c = 2459601.7796(9)$. We only used these to improve the linear ephemeris of the system.

The primary star has, according to the ARIADNE fit, a temperature of $T_1 = 5760(30)$ K and radius $R_1 = 1.26(2)\,R_\odot$. The spectral fit by A. Bieryla at FLWO@TRES available on the ExoFOP database gives $T_1 = 5720(50)$ K, $\log g = 4.39(10)$, [Fe/H] = 0.00(8) and a rotational velocity of $v\sin i = 12.2(5)$ km/s with a corresponding rotational period of $P_{rot} = 5.24(23)$ d, which is
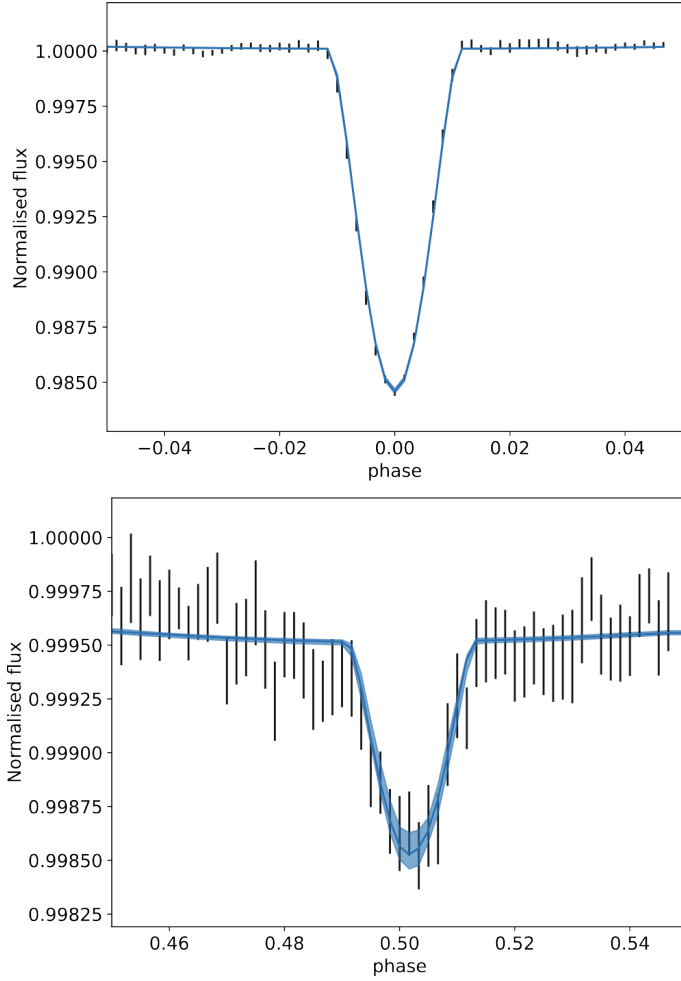
Fig. 9. Light curve of TOI-1615. We can see the partial primary eclipse in the top panel and very shallow secondary eclipse in the bottom panel.
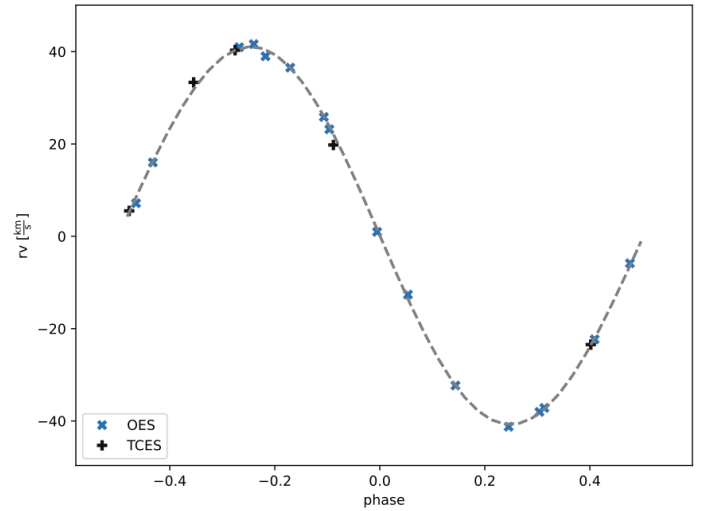

Fig. 10. Radial velocity curve of TOI-1615 obtained by OES and TCES after correction for zero-point velocities with our best-fit model showing a circular orbit. Errors of the data points are smaller than the markers.
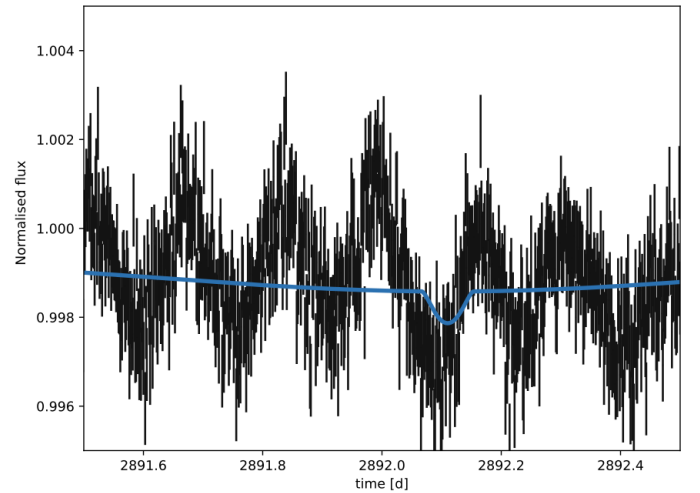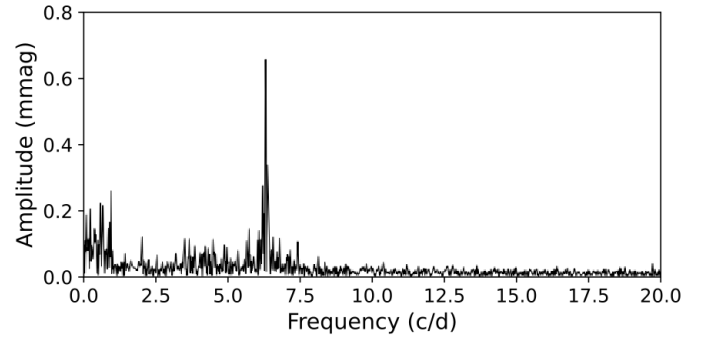

Fig. 11. Delta Scuti pulsations of TOI-1615A. Top panel: frequency-amplitude spectrum of the residual fluxes after removing the binary solution. Bottom panel: zoomed-in view of pulsation in the normalized TESS light curve; blue curve corresponds to binary fit showing the depth of the secondary eclipse in comparison to the pulsation amplitude.

similar to both the orbital period and the period of photometric variability.

In Fig. 13, we can see the resulting fit of the binned light curve. The fit is degenerate in i, R_2/R_1 and $(R_1 + R_2)/a$ with only a lower bound on the secondary radius $R_2 > 0.09\,R_\odot$ and a crude estimate of semi-major axis $a = 13.7(20)\,R_\odot$. As we did not detect the secondary eclipse, it is best to consider the system just as a spectroscopic binary with known inclination $i = 84(2)°$. If we use the ARIADNE-MIST model, we obtain masses for the components of $M_1 = 0.96(7)\,M_\odot$ – a G2IV star; and $M_2 = 0.178(15)\,M_\odot$ – most probably an M4V star. The full set of estimated parameters can be found in Table 5.

Next, we return to the nature of the photometric variability. The variability certainly does not originate from the secondary, given that the amplitude of 2% is much higher than the light contribution of the secondary itself. The variability can be detected in broadband (with a sensitivity level in range of 400–700 nm) SuperWASP photometry data (Pollacco et al. 2006) from December 2006 – May 2007 with an amplitude of 0.0125^m and a period of $P_{SW} = 5.62\,d$, as well as with half this period and an amplitude of 0.0066^m. The period is slightly longer than the one in the TESS data; the latter was, however, determined from just one month-long series of data in Sector 48. The amplitude is slightly lower in SuperWASP data with a more prominent harmonic component. In Sector 21, the variability has

a more pronounced double peak nature evolving across the sector. We considered the following options to explain this:

– pulsations of the primary;
– starspots on the primary;
– a blend with a background variable.
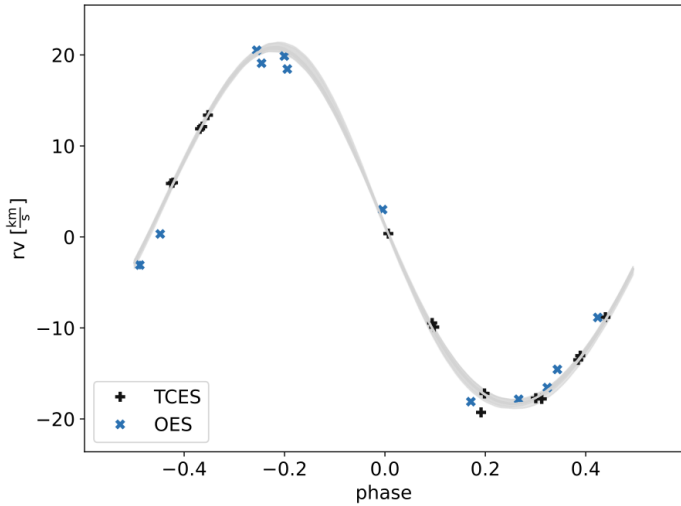
Fig. 12. Radial-velocity curve of TOI-1788 obtained by OES and TCES after correction for instrumental zero-point shift. The shaded region demonstrates uncertainty in model posteriors, and errors of measured data points are smaller than the symbols. The higher than expected scatter is caused by stellar spots on the primary.

We did not notice another set of spectral lines in the TOI-1788 spectra, nor did we notice a secondary bump in the cross-correlation function. This, together with the imaging, rules out a background variable that could contribute enough light to explain the variability. Pulsations of the primary are not expected. In this temperature range, one would only expect faster, solar-type oscillations with periods up to a few minutes and low amplitude. Star spots are thus the most probable source of this variability, which is further supported by the presence of the double harmonic frequency. The difference between the photometric periods and the orbital one can be explained by differential rotation of a spin-synchronized primary with a large spotted region near one of the star poles. We tried to check for changes in depth or duration of the primary eclipses, but given their shallow nature we were not able to detect any changes conclusively. We also note that the stellar spots are the most probable source of higher scatter in radial velocities in Fig. 12, just as the corresponding errors of the data points suggest.

Finally, the binary has a possible outer companion with the designation 2MASS 10403438+3543348 at a distance of approximately 13″, a projected relative velocity of about $\mu = 0.49$ mas/yr, and a reported difference in parallax of only $0.14(11)$ mas. At the distance of the sources, the projected separation is $d \approx 3000$ au and the projected relative velocity is $v \approx 0.54$ km/s, which is consistent with a companion on an orbit of a few hundred thousand years. Both the GAIA color index $BP - RP = 2.46$ and apparent magnitude $G = 16.688$ suggest an M3 main-sequence dwarf star.

6. Discussion

We present parameters for five eclipsing binaries that are also single-lined spectroscopic binaries. To obtain the primary star parameters, we used SED modeling; the radii and temperatures obtained thus depend on the precision of the Gaia DR2 parallaxes used and the contamination of the photometry by other sources. Our stars are fainter than $G < 8$ and lie in relatively sparse fields, thus avoiding the known systematic issues outlined
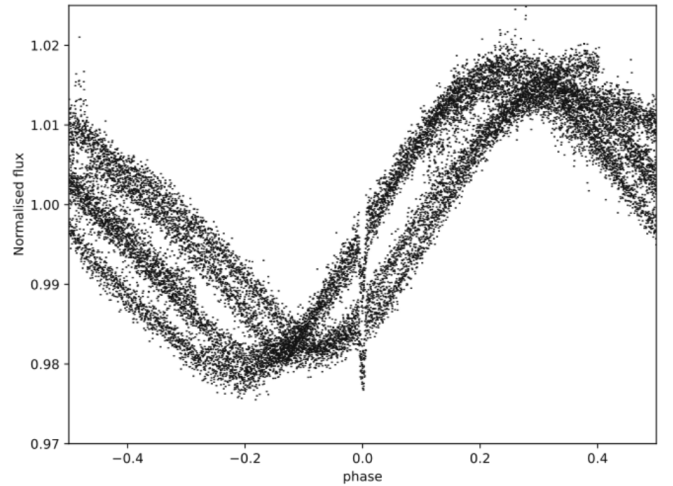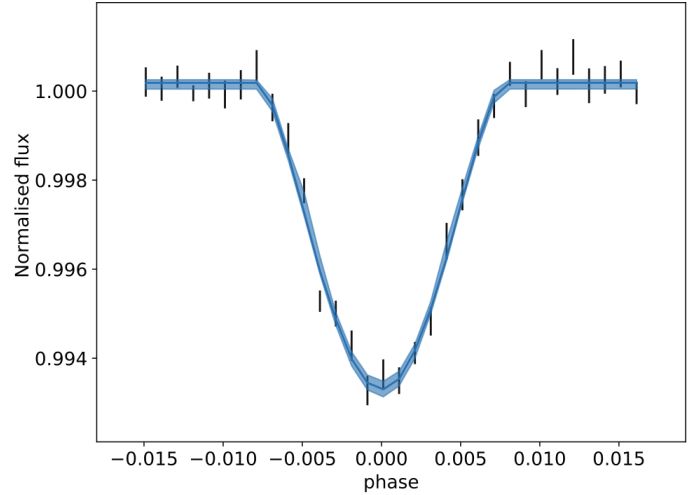

Fig. 13. Light curve of TOI-1788. In the top panel, we can see the primary eclipse. We do not detect any secondary eclipses. Rotation-related changes in the original TESS-SPOC light curve shown in the orbital phase are located in the bottom panel.

on the Gaia website[6], but we did not investigate the other issues raised in Lindegren et al. (2018).

We fit the extinction, which is rather small for all systems. To rule out contamination by other point sources close to the targets, we used the astrometric solution excess error RUWE in Gaia and speckle imaging in the Exofop archive, where available. A high RUWE value of >1.4 is a good indicator of binarity; however, a smaller value does not rule out possible companion(s). Beck et al. (2024) showed that $\approx 40\%$ of binaries in the ninth catalog of spectroscopic binary orbits (Pourbaix et al. 2004) have values of RUWE < 1.4, mostly in cases of targets with shorter orbital periods below 100 d. For TOI-1615, there was no further imaging available. In the other cases, we found reasonable contrast down to $0.1''–0.2''$, which at the distance of the targets gives a region of radius $15–30$ au. Another bound star could still orbit the systems on an orbit up to ≈ 100 y. If we consider a mass ratio of $q = 0.3$, the third component would cause radial-velocity variability in the central binary system with a semi-amplitude of about $2–3$ km/s, which can easily be missed in our data with time spans of a few years as well as in the Gaia astrometry. Also, the change in times of eclipses is quite small in this case – just
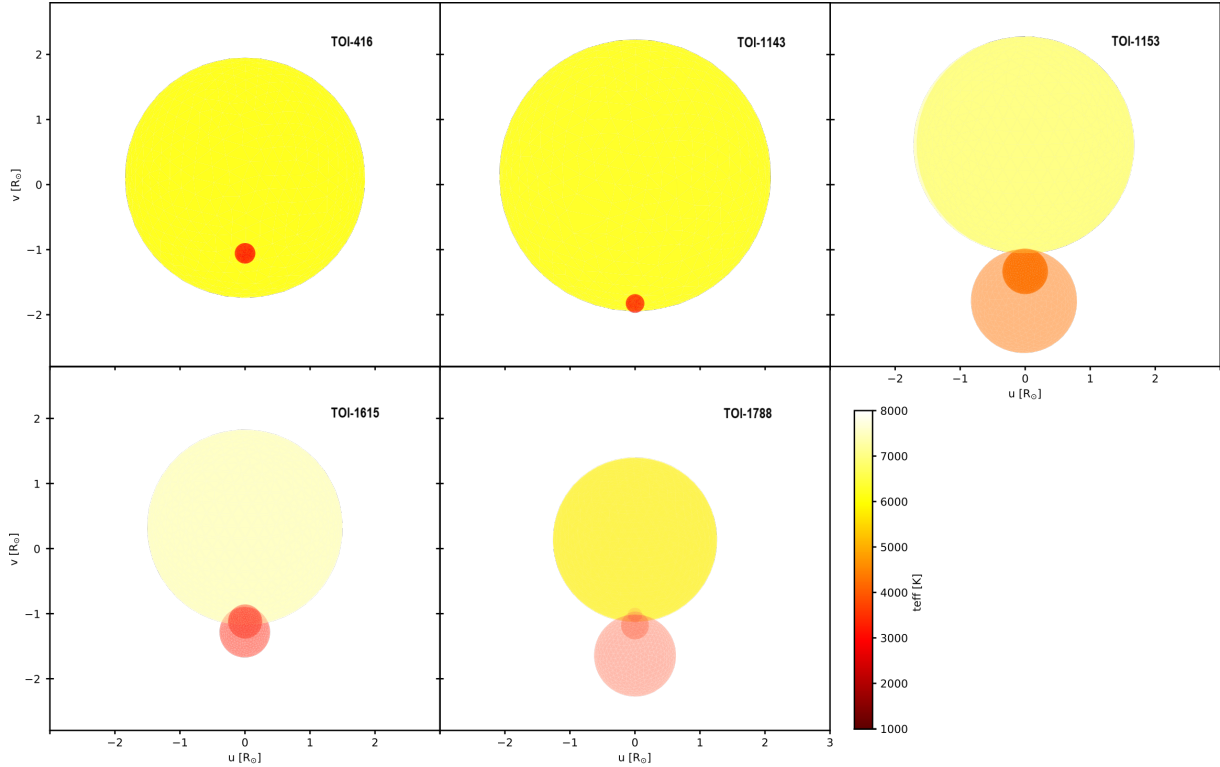
---

[6] https://www.cosmos.esa.int/web/gaia/dr2-known-issues#AstrometryConsiderations

Fig. 14. Family portraits of the systems in the middle of the primary eclipse. The secondary moves horizontally across the disk of the primary. Shading for the secondary corresponds to the uncertainty in the posterior values of secondary radius. All systems are drawn to the same scale within boxes that are $6\,R_\odot$ in length.

a five minute or less change in one year of observations. Thus, it would be preferable to place tighter constraints on the possible companions with more sensitive imaging or long-term eclipse time monitoring in order to be certain for the well-described systems TOI-416 and TOI-1143. Another issue for TOI-1153, TOI-1615, and TOI-1788 is that the lack of knowledge of the secondary parameters hinders us in the removal of its contribution to the SED. Here, we used the expected values for stars of the same mass from Pecaut & Mamajek (2013) instead of our own radius and temperature estimates with large uncertainties.

Another important point is the use of tabulated values of limb-darkening coefficients, albedos, gravity brightening coefficients, and beaming coefficients for the photometry model. As can be seen in the works of Claret (2017, 2001, 2003), and Claret et al. (2020), respectively, limb darkening is a well-studied effect with observational verification of the models compared to the other coefficients, where precise observations are in short supply. Limb darkening manifests in the shape of the eclipse intertwined with the eclipse geometry, so we opted to use the tables. In the case of albedos and gravity brightening, there is also an abrupt change of the values around the transition from a convective envelope to a radiative one in the $T = 6000-7000\,K$ range, which is relevant for four of our targets. We used fixed values of these parameters as outlined in Sect. 4. This could cause model-dependent errors with secondary eclipse depth, secondary temperature being the most vulnerable. We discuss the beaming coefficients in a later section.

6.1. Radius–mass–temperature relationships

One of the most important uses of our work is the calibration of fundamental stellar parameters for dwarf stars. In Fig. 15, we

can see the radius-mass relation for the secondaries from our systems together with dwarf stars parameters from Chaturvedi et al. (2018, references therein,) and Swayne et al. (2023), which contains the work of the EBLM project. We can see that for stars with radiative interiors with masses above $0.35\,M_\odot$, the observed radii are inflated in comparison with the MIST stellar models' zero-age main sequence for a metallicity of $[Fe/H] = 0.0$. For the fully convective stars, $M < 0.35\,M_\odot$, the model describes the measurements well. Our points with robust measurements for TOI-416 and TOI-1143 lie amongst the other known stars in the R–M diagram close to the theoretical prediction.

The temperature–mass diagram in Fig. 16 shows a scatter with most of the points colder than the model, except for the TOI-1143, which is clearly above. However, considering the error bars, the measured and model values agree within a few hundred kelvin. We can also use these relations to predict the expected radii and temperatures for the other three secondaries – $R_2 = 0.65(4)\,R_\odot$, $T_2 = 4300(200)\,K$ for TOI-1153B; $R_2 = 0.50(2)\,R_\odot$, $T_2 = 3750(150)\,K$ for TOI-1615B; and $R_2 = 0.18(2)\,R_\odot$, $T_2 = 3150(150)\,K$ for TOI-1788B.

6.2. Beaming and boosting

As described in Table 4, we have three systems with beaming amplitudes estimated: TOI-416, TOI-1153, and TOI-1615. We can compare these with the theoretical predictions and the relation and values according to Faigler & Mazeh (2011) and Claret et al. (2020). Our parameter B is related to the beaming coefficients in TESS band B_T in tables by Claret et al. (2020) in the following way:

$$B = l_1 B_{T,1} \frac{K_1}{c} - l_2 B_{T,2} \frac{K_2}{c} = \left(l_1 B_{T,1} - \frac{(1-l_1)B_{T,2}}{q} \right) \frac{K_1}{c}, \qquad (9)$$
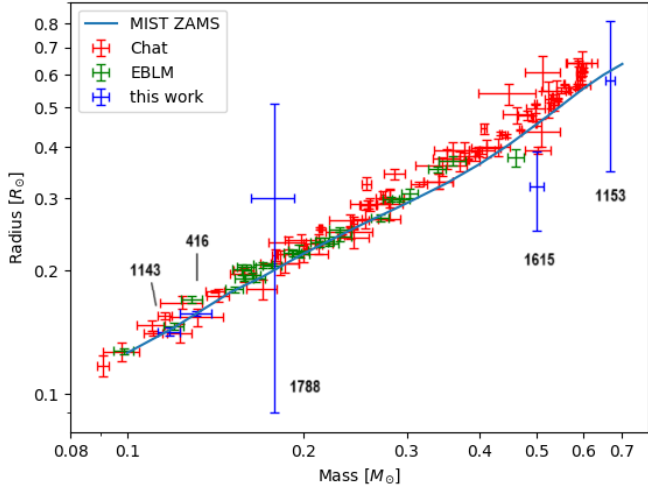
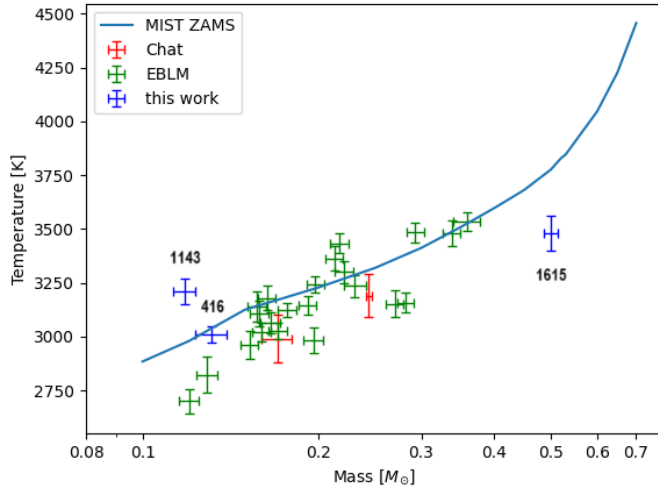**Fig. 15.** Radius–mass diagram of dwarf stars. Stars from Chaturvedi et al. (2018) and references therein are shown in red, stars from the EBLM project Swayne et al. (2023) in green, and our secondaries in blue. The blue line denotes the zero-age main sequence from the MIST stellar models for the metallicity [Fe/H] = 0.0.

Fig. 16. Temperature–mass diagram of dwarf stars. Stars from Chaturvedi et al. (2018) and references therein are shown in red, stars from the EBLM project Swayne et al. (2023) in green, and our secondaries with temperature estimates in blue. The blue line denotes the zero-age main sequence from the MIST stellar models for metallicity [Fe/H] = 0.0.

where l_i is the relative light contribution of the component in the pass band, K_i is the semi-amplitude of the radial velocities of this component, and q is the binary-mass ratio. Here, it is important to note that the contribution of the second term tend to be negligible as the mass ratio becomes smaller; for FGKM stars, it approximately holds $R \propto M$, and so l_2/l_1 decreases faster than q^2 given by the additional decrease also in temperature. We can see a comparison between the theoretically expected values, B_{exp}, and the measured ones, B_{meas}, in Table 6. In the case of the well-characterized TOI-416, the values agree nicely. For TOI-1153 and TOI-1615, the measured values are significantly lower, pointing to the issues with parameter estimation. This discrepancy can be explained only if we underestimated the temperature and radius values of the secondaries in these systems. Reintroducing support for beaming into a future version of PHOEBE is

Table 6. Beaming amplitudes for TOI-416, TOI-1153, and TOI-1615.

Target	TOI-416	TOI-1153	TOI-1615
$B_{T,1}$	3.05(3)	2.75(5)	2.64(3)
$B_{T,2}$	6.2(3)	6.2(5)	5.6(1)
l_1	0.99978(3)	>0.990	0.998(1)
$B_{\text{exp}} \cdot 10^5$	11.3(2)	39.5(15)	35.5(6)
$B_{\text{meas}} \cdot 10^5$	10.9(14)	24.3(25)	25.6(92)

planned (DJ, priv. comm.), requiring the user to manually provide the beaming coefficients. This could be used as an additional constraint to break the degeneracy in grazing eclipses, but the beaming coefficients strongly depend on temperature, which is not easy to determine for the secondary.

6.3. Grazing eclipses

As we can see from Fig. 14, grazing eclipses lead to degeneracy in the stellar radii and inclination, giving the same photometric profile during the eclipse for vastly different radii of the stars. We now look more closely at the limiting case of just grazing eclipses. We assume a circular orbit for the demonstration. The duration of the eclipse (T) can be derived from the orbital speed (v) and the distance between centers of the secondary during first and last contact ($2L$). For the length (L), we have the following from the right triangle:

$$L^2 + a^2 \cos^2 i = (R_1 + R_2)^2. \tag{10}$$

If we use an equation for the orbital speed $v = 2\pi a/P$, we obtain a relation between the directly measurable quantity T/P and the derived ones:

$$\left(\frac{\pi T}{P}\right)^2 + \cos^2 i = \left(\frac{R_1 + R_2}{a}\right)^2. \tag{11}$$

Similarly, for the separation of stellar disk centers ($H(t)$) in time measured from the middle of the eclipse, we can obtain an equation:

$$H^2(t) = (R_1 + R_2)^2 + (2\pi a)^2 \left[\left(\frac{t}{P}\right)^2 - \left(\frac{T}{2P}\right)^2\right]. \tag{12}$$

The depth of the eclipse (δ) under the assumption of homogeneous disks can be expressed as

$$\delta = \frac{A}{\pi R_1^2 + \pi \alpha R_2^2}, \tag{13}$$

where A is the covered area of the primary and α is the surface-brightness ratio of the secondary to the primary. The area of the thin lens in the case of a grazing eclipse can be expressed as

$$A = \frac{2}{3}\theta_1^3 R_1^2 + \frac{2}{3}\theta_2^3 R_2^2, \tag{14}$$

with an error term in θ_i^5, where θ_i are the angles between the end of the lens and its center as seen from the center of the respective stellar disks. From the common chord, we have the equation $R_1 \sin\theta_1 = R_2 \sin\theta_2$, and from the segment between the stellar centers we have $R_1 \cos\theta_1 + R_2 \cos\theta_2 = H(t = 0)$. Using the Taylor series, we obtain

$$R_1\theta_1 = R_2\theta_2, \quad R_1\frac{\theta_1^2}{2} + R_2\frac{\theta_2^2}{2} = R_1 + R_2 - H(t = 0). \tag{15}$$

If we define $E = R_1 + R_2 - H$ (which is our limiting quantity), we obtain the angles

$$\theta_1 = \sqrt{\frac{2R_2 E}{R_1(R_1 + R_2)}}, \quad \theta_2 = \sqrt{\frac{2R_1 E}{R_2(R_1 + R_2)}}. \quad (16)$$

We can see that for $R_2 < R_1$ is $\theta_2 > \theta_1$, and we need $E \ll R_2 < R_1$ for the approximation to hold. Substituting into Equations (14) and (13), we obtain

$$\delta = \frac{2}{3\pi} \left(\frac{2E}{R_1 + R_2}\right)^{\frac{3}{2}} \frac{\sqrt{R_1 R_2}(R_1 + R_2)}{R_1^2 + \alpha R_2^2}. \quad (17)$$

From Equation (12), we can derive the approximate relation

$$E = (2\pi a)^2 \frac{1}{2(R_1 + R_2)} \left[\left(\frac{T}{2P}\right)^2 - \left(\frac{t}{P}\right)^2\right]. \quad (18)$$

If we substitute this into the previous equation, we obtain the time dependence of the depth

$$\delta(t) = \frac{2}{3\pi} \left(\frac{2\pi a}{R_1 + R_2}\right)^3 \frac{\sqrt{R_1 R_2}(R_1 + R_2)}{R_1^2 + \alpha R_2^2} \left[\left(\frac{T}{2P}\right)^2 - \left(\frac{t}{P}\right)^2\right]^{\frac{3}{2}}. \quad (19)$$

We thus obtain Equations (19) and (11) for the eclipse depth as a function of time t ($|t| < T/2$) and its duration: equations relating two measurable quantities and the three unknown parameters i, R_2/R_1 and $(R_1 + R_2)/a$.

An easy way to check for the presence of degeneracy in a shallow eclipse is to estimate the fractional width of the eclipse profile at half the depth ξ, that is, the ratio of the full width at half minima (FWHM) to the duration T between first and last contact. ξ should take values from close to $\xi \approx 1.0$ in the case of total eclipses (in practice slightly lower due to limb darkening) with trapezoidal shapes, to $\xi \doteq 0.608$ in the degenerate case with a more V-shaped eclipse.

As an example, we consider a system with an eclipse of maximal depth of $\delta_{\max} = 0.0064$ and duration of $T = 0.02P$. Using PHOEBE, we took a primary with a radius of $R_1 = 1.67\,R_\odot$ and a temperature of $T_1 = 7000\,K$ akin to the F1V star and tried to obtain the eclipse depth and duration for a sample of main-sequence secondaries (adjusting the temperature for the given radius) on $P = 10\,d$ orbit. We first fixed the inclination and then adjusted $(R_1 + R_2)/a$ to fit the duration and, subsequently, R_2/R_1 to fit the depth. The resulting light curve in the Johnson V band in Fig. 17 shows a quick change from the trapezoidal shape for the minimal possible value of $R_2/R_1 = 0.08$ at $i = 87.05°$ and $(R_1 + R_2)/a = 0.0789$ to the degenerate shape at $R_2/R_1 = 0.096$, $i = 84.55°$, $(R_1 + R_2)/a = 0.112$. For bigger radii of the secondary, the shape of the primary eclipse was practically indistinguishable all the way up to $R_2 = R_1$ at $i = 80.8°$ and $(R_1 + R_2)/a = 0.1708$.

The visible difference between the light curves was in the presence of a deepening secondary eclipse with increasing temperature of the secondary. This difference, however, can be lost in the case of an even slightly eccentric orbit. Therefore, the only usable difference is the presence of ellipsoidal variations that strengthen as the stars become closer in size. We demonstrated the use of ellipsoidal variation in breaking the degeneracy in the case of TOI-1153. In the case of TOI-1788, there was no helping factor given the spot-associated variability of the star. Another option to break the degeneracy is to have either an estimate for the secondary radius from the spectral-energy-distribution fit – feasible mostly when the secondary is an evolved giant star – or
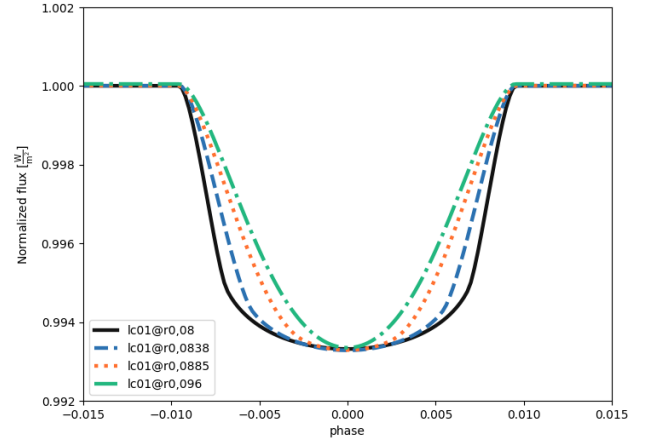
Fig. 17. Light curve of a primary eclipse with fixed depth and duration. We demonstrate the changing shape during transition from total eclipse to the degenerate grazing case. From the outside curve inward, we used values $R_2/R_1 = [0.0800, 0.0838, 0.0885, 0.0960]$. For $R_2/R_1 > 0.1$, the change of shape is indistinguishable from the $R_2/R_1 = 0.0960$ case.

to have an SB2 binary, thus obtaining a semi-major axis from the radial velocities of both components and solving for i and R_2 from the depth and duration. However, it is still necessary to use the spectral-energy-distribution fit to obtain the primary radius. One may also wonder whether it is possible to break the degeneracy using the information about stellar rotation from spectra. We can quickly dismiss this option with an example. If we consider the difference between $84°$ and $85°$ inclinations in our systems, the difference between the sines of these values is just 1.7×10^{-3}. Even under the assumption that the orbital and rotational axis of the primary are colinear on a $<1°$ scale (which we deem dubious), we would need the orbital period, projected rotational velocity, and primary radius all measured with a relative precision on the order of 10^{-3} or better, which is unfeasible.

7. Conclusions

We obtained the orbital elements and physical parameters of five eclipsing binary stars identified by the TESS mission and observed for radial-velocity follow-up from Ondřejov Observatory, Tautenburg Observatory and others. Two of the systems are well described: TOI-416, consisting of an F6 star leaving the main sequence and an M5V secondary on a circular orbit; and TOI-1143, consisting of an F6 sub-giant and an M5.5V dwarf on an eccentric orbit with an outer companion. The parameters of these systems, with a precision level of about 2% in radii and 5% in masses, can be used in the calibration of the stellar models of dwarf stars.

TOI-1153 ($\approx$F2+K6), with large ellipsoidal variation; TOI 1615 ($\approx$A9+M3), with a pulsating primary; and TOI-1778 ($\approx$G2+M5), with a suspected outer M3 companion are somewhat lacking in the full description given the poor constraints on the photometry-related parameters due to grazing eclipses. We conclude that exoplanetary candidates are a rich source of eclipsing binaries of two types: fully eclipsing, low-mass stars in front of mid- to early-type primaries, allowing for a good description of the system; and grazing systems with larger mass ratios that provide only poor solutions for the photometric quantities, and thus also system parameters without further model-dependent assumptions.

References

Alam, S., Albareti, F. D., Allende Prieto, C., et al. 2015, ApJS, 219, 12
Allard, F., Homeier, D., Freytag, B., & Sharp, C. M. 2012, EAS Publ. Ser., 57, 3
Alton, K. B., & Stępień, K. 2018, Acta Astron., 68, 449
Bailer-Jones, C. A. L., Rybizki, J., Fouesneau, M., Mantelet, G., & Andrae, R. 2018, AJ, 156, 58
Baraffe, I., Homeier, D., Allard, F., & Chabrier, G. 2015, A&A, 577, A42
Beck, P. G., Grossmann, D. H., Steinwender, L., et al. 2024, A&A, 682, A7
Bianchi, L., Herald, J., Efremova, B., et al. 2011, Ap&SS, 335, 161
Breger, M., Hutchins, J., & Kuhi, L. V. 1976, ApJ, 210, 163
Buchhave, L. A., Bakos, G. Á., Hartman, J. D., et al. 2010, ApJ, 720, 1118
Campbell, B., Walker, G. A. H., & Yang, S. 1988, ApJ, 331, 902
Castelli, F., & Kurucz, R. L. 2003, in Modelling of Stellar Atmospheres, eds. N. Piskunov, W. W. Weiss, & D. F. Gray, 210, A20
Chabrier, G. 2003, PASP, 115, 763
Chabrier, G., & Baraffe, I. 1997, A&A, 327, 1039
Chabrier, G., Baraffe, I., Phillips, M., & Debras, F. 2023, A&A, 671, A119
Chambers, K. C., Magnier, E. A., Metcalfe, N., et al. 2016, ArXiv e-prints [arXiv:1612.05560]
Chaturvedi, P., Sharma, R., Chakraborty, A., Anandarao, B. G., & Prasad, N. J. S. S. V. 2018, AJ, 156, 27
Choi, J., Dotter, A., Conroy, C., et al. 2016, ApJ, 823, 102
Churchwell, E., Babler, B. L., Meade, M. R., et al. 2009, PASP, 121, 213
Claret, A. 2001, MNRAS, 327, 989
Claret, A. 2003, A&A, 406, 623
Claret, A. 2017, A&A, 600, A30
Claret, A., Cukanovaite, E., Burdge, K., et al. 2020, A&A, 641, A157
Conroy, K. E., Kochoska, A., Hey, D., et al. 2020, ApJS, 250, 34
Duchêne, G., Oon, J. T., De Rosa, R. J., et al. 2023, MNRAS, 519, 778
Duck, A., Martin, D. V., Gill, S., et al. 2023, MNRAS, 521, 6305
Faigler, S., & Mazeh, T. 2011, MNRAS, 415, 3921
Foreman-Mackey, D., Hogg, D. W., Lang, D., & Goodman, J. 2013, PASP, 125, 306
Frandsen, S., & Lindberg, B. 1999, in Astrophysics with the NOT, eds. H. Piirola, V. Karttunen, 71
Fűrész, G. 2008, PhD Thesis, University of Szeged, Hungary
Gaia Collaboration (Brown, A. G. A., et al.) 2016, A&A, 595, A2
Gaia Collaboration (Brown, A. G. A., et al.) 2018, A&A, 616, A1
Gaia Collaboration (Arenou, F., et al.) 2023, A&A, 674, A34
Gandolfi, D., Parviainen, H., Fridlund, M., et al. 2013, A&A, 557, A74
Gandolfi, D., Parviainen, H., Deeg, H. J., et al. 2015, A&A, 576, A11
Grundahl, F., Fredslund Andersen, M., Christensen-Dalsgaard, J., et al. 2017, ApJ, 836, 142
Hauschildt, P. H., Allard, F., & Baron, E. 1999, ApJ, 512, 377
Henden, A., & Munari, U. 2014, Contrib. Astron. Obs. Skalnate Pleso, 43, 518
Høg, E. 2000, in Encyclopedia of Astronomy and Astrophysics, ed. P. Murdin, 2862
Howell, S. B., Everett, M. E., Sherry, W., Horch, E., & Ciardi, D. R. 2011, AJ, 142, 19
Husser, T. O., Wende-von Berg, S., Dreizler, S., et al. 2013, A&A, 553, A6
Hut, P. 1981, A&A, 99, 126
Kabáth, P., Skarka, M., Sabotta, S., et al. 2020, PASP, 132, 035002
Kharchenko, N. V. 2001, Kinematika i Fizika Nebesnykh Tel, 17, 409
Kraft, R. P. 1967, ApJ, 150, 551
Kunder, A., Kordopatis, G., Steinmetz, M., et al. 2017, AJ, 153, 75
Kurucz, R. L. 1993, VizieR Online Data Catalog: VI/39
Lenz, P., & Breger, M. 2005, Commun. Asteroseismol., 146, 53
Lindegren, L., Hernández, J., Bombrun, A., et al. 2018, A&A, 616, A2
Maxted, P. F. L. 2016, A&A, 591, A111
Maxted, P. F. L., Triaud, A. H. M. J., & Martin, D. V. 2023, Universe, 9, 498
Narita, N., Fukui, A., Kusakabe, N., et al. 2019, J. Astron. Telesc. Instrum. Syst., 5, 015001
Offner, S. S. R., Moe, M., Kratter, K. M., et al. 2023, ASP Conf. Ser., 534, 275
Parsons, S. G., Gänsicke, B. T., Marsh, T. R., et al. 2018, MNRAS, 481, 1083
Pathania, A., & Medupe, T. 2012, Ap&SS, 338, 127
Paunzen, E. 2015, A&A, 580, A23
Pecaut, M. J., & Mamajek, E. E. 2013, ApJS, 208, 9
Pollacco, D. L., Skillen, I., Collier Cameron, A., et al. 2006, PASP, 118, 1407
Pourbaix, D., Tokovinin, A. A., Batten, A. H., et al. 2004, A&A, 424, 727
Prša, A. 2018, Modeling and Analysis of Eclipsing Binary Stars; The Theory and Design Principles of PHOEBE (Bristol: IOP Publishing)
Prša, A., Conroy, K. E., Horvat, M., et al. 2016, ApJS, 227, 29
Prša, A., Kochoska, A., Conroy, K. E., et al. 2022, ApJS, 258, 16
Ribas, I. 2003, A&A, 398, 239
Ricker, G. R., Winn, J. N., Vanderspek, R., et al. 2015, J. Astron. Telesc. Instrum. Syst., 1, 014003
Schlegel, D. J., Finkbeiner, D. P., & Davis, M. 1998, ApJ, 500, 525
Scott, N. J., Howell, S. B., Horch, E. P., & Everett, M. E. 2018, PASP, 130, 054502
Skrutskie, M. F., Cutri, R. M., Stiening, R., et al. 2006, AJ, 131, 1163
Stassun, K. G., Oelkers, R. J., Pepper, J., et al. 2018, AJ, 156, 102
Swayne, M. I., Maxted, P. F. L., Triaud, A. H. M. J., et al. 2023, MNRAS, submitted [arXiv:2312.11339]
Telting, J. H., Avila, G., Buchhave, L., et al. 2014, Astron. Nachr., 335, 41
Triaud, A. H. M. J., Hebb, L., Anderson, D. R., et al. 2013, A&A, 549, A18
Vines, J. I., & Jenkins, J. S. 2022, MNRAS, 513, 2719
Wanderley, F., Cunha, K., Souto, D., et al. 2023, ApJ, 951, 90
Wright, E. L., Eisenhardt, P. R. M., Mainzer, A. K., et al. 2010, AJ, 140, 1868
Zechmeister, M., Köhler, J., & Chamarthi, S. 2021, Astrophysics Source Code Library [record ascl:2108.006]
Zucker, S., Mazeh, T., & Alexander, T. 2007, ApJ, 670, 1326
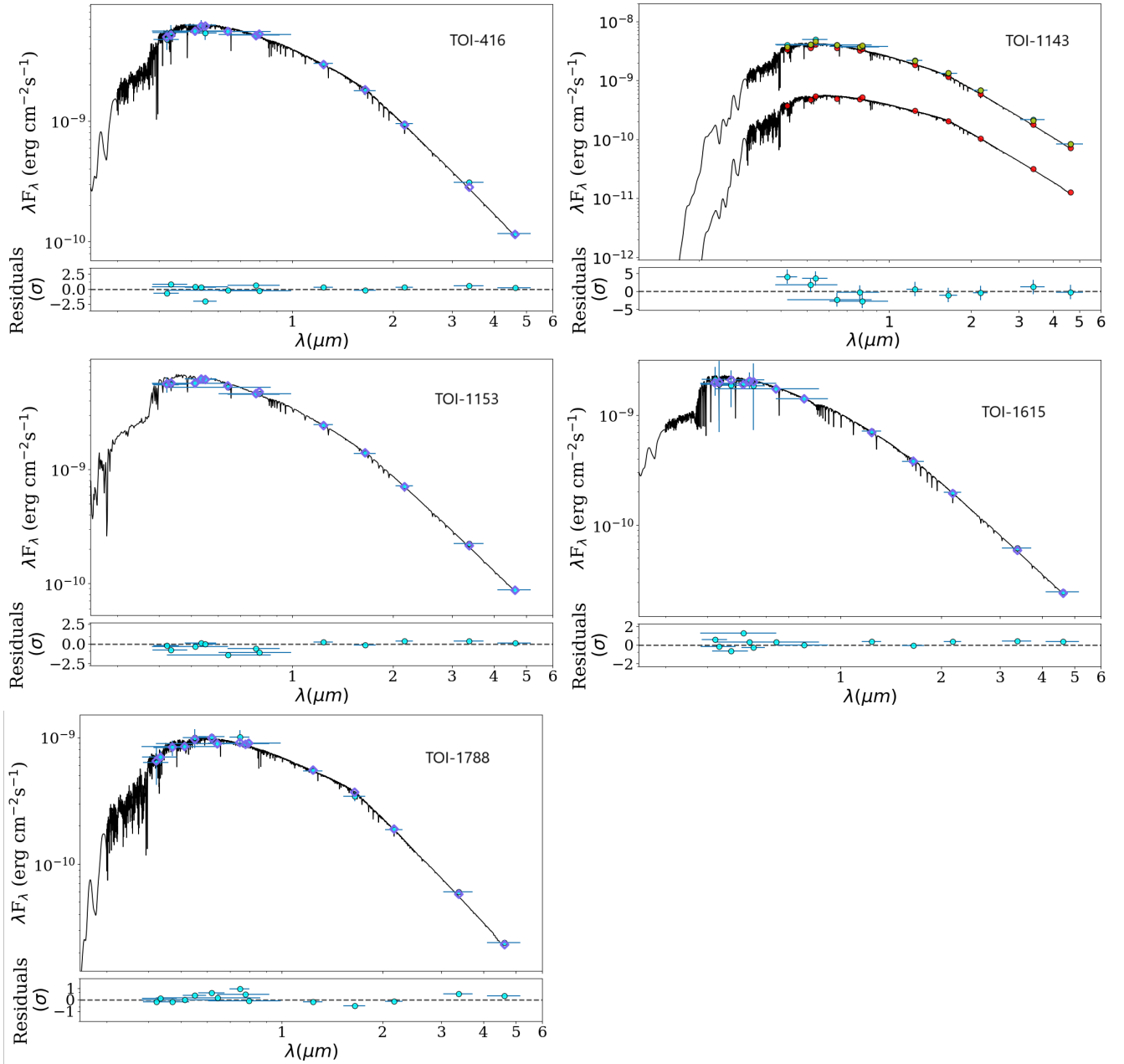
Appendix A: SED models

Fig. A.1. SED fits of primary stars in our systems after subtracting the fluxes of the secondaries. In the case of TOI-1143, we simultaneously modeled both primary stars and fainter companions visible in the speckle imaging, assuming the same distance and contrast $\Delta I = 2.07(10)$.

Appendix B: Measured radial velocities

Table B.1. Relative radial velocities of the target stars.

BJD	RV (km/s)	Err (km/s)	BJD	RV (km/s)	Err (km/s)	BJD	RV (km/s)	Err (km/s)
TOI-416 (OES)			TOI-1143 (OES)			TOI-1615 (OES)		
2458523.2280	19.623	0.123	2459044.4553	-0.062	0.085	2458892.3214	73.955	0.119
2458523.2598	21.790	0.129	2459044.5457	0.568	0.101	2458892.5952	68.857	0.172
2458529.2246	12.212	0.084	2459062.3901	12.655	0.087	2458895.2921	24.748	0.559
2458530.2746	20.736	0.183	2459068.5359	9.758	0.092	2458898.4056	-5.719	0.221
2458530.2959	20.189	0.183	2459070.5436	16.930	0.117	2458898.4425	-4.858	0.124
2458531.2708	18.531	0.153	2459071.5622	16.471	0.115	2458901.3592	19.702	0.140
2458531.3025	16.264	0.117	2459075.5707	8.001	0.205	2458924.3690	58.159	0.104
2458532.2923	8.149	0.116	2459089.5950	0.287	0.128	2458925.3568	0.000	0.095
2458532.3241	7.351	0.157	2459104.5956	16.941	0.080	2458926.4010	10.002	0.100
2458533.2525	0.000	0.048	2459105.5086	15.585	0.099	2458928.3504	55.504	0.099
2458533.2947	0.240	0.052	2459106.5041	14.089	0.077	2458930.6063	26.474	0.353
2459246.2463	17.656	0.222	2459108.4451	8.961	0.079	2458935.5544	73.286	0.111
TOI-416 (FIES)			2459120.5219	6.360	0.113	2458936.5892	33.280	0.105
2458513.3854	-0.011	0.011	2459175.6687	9.199	0.109	2458937.5765	-8.927	0.100
2458514.3988	6.396	0.010	TOI-1143 (TRES)			2458946.6006	39.485	0.101
2458515.4654	16.773	0.018	2458820.0399	-14.525	0.063	2458947.5723	71.317	0.159
2458517.3940	19.634	0.014	2458837.0365	1.096	0.058	2459242.2406	48.322	0.168
2458518.4782	9.815	0.012	2458848.0285	1.514	0.058	TOI-1615 (TLS)		
2458522.4553	16.610	0.010	2458853.9270	-14.484	0.075	2458855.4712	8.881	0.245
2458523.4578	22.160	0.012	2458859.9602	0.000	0.058	2458860.6821	71.814	0.240
TOI-416 (SONG)			2458871.9689	-1.904	0.028	2458864.3191	64.048	0.234
2458512.3326	23.078	0.005	2458876.0529	-14.264	0.081	2458865.3602	50.574	0.244
2458513.3293	20.786	0.004	2458878.8815	0.721	0.042	TOI-1788 (OES)		
2458514.3292	26.586	0.006	2458885.9672	-10.306	0.071	2458959.4386	36.293	0.177
2458515.3316	36.470	0.004	2458888.9593	-6.892	0.052	2458960.4531	20.843	0.117
2458516.3566	42.637	0.005	TOI-1153 (TLS)			2458961.3928	-0.261	0.168
2458517.3148	40.522	0.004	2458923.5398	-60.720	0.250	2458963.4300	18.166	0.111
2458518.3412	32.327	0.005	2458923.5505	-60.010	0.380	2458964.5088	36.929	0.206
TOI-1143 (OES)			2458923.5613	-59.980	0.180	2458967.5505	1.288	0.111
2458892.4386	16.322	0.086	2459067.5052	-83.650	0.350	2458975.4397	37.716	0.299
2458892.5283	16.234	0.083	2459068.5750	-53.510	0.190	2459191.6999	0.000	0.098
2458895.3833	9.790	0.053	2459094.4663	5.190	0.230	2459246.4524	14.752	0.463
2458901.3009	14.855	0.072	2459095.5200	-16.310	0.240	2459983.4748	8.991	0.095
2458924.4007	16.866	0.083	2459099.5398	-18.110	0.370	2460004.4211	3.283	0.147
2458925.3960	16.375	0.056	2459100.4393	4.750	0.230	2460065.3497	38.356	0.143
2458930.3286	5.452	0.108	2459100.6216	5.110	0.270	2460087.3911	32.868	0.399
2458930.4164	5.111	0.113	2459101.6213	-19.350	0.270	TOI-1788 (TLS)		
2458931.3062	1.785	0.059	2459177.5857	-37.320	0.280	2459177.6200	25.944	0.364
2458931.3936	1.609	0.073	2459177.5967	-36.440	0.560	2459177.6417	26.178	0.257
2458932.3371	-0.178	0.051	2459178.6741	2.030	0.510	2459265.5971	4.600	0.175
2458932.4288	0.000	0.046	2459179.4647	0.780	0.740	2459265.6188	4.152	0.135
2458933.3227	3.349	0.057	2459179.4758	0.790	0.660	2459268.5539	27.443	0.161
2458933.4101	4.057	0.056	2459212.5910	-81.020	0.310	2459270.4744	14.425	0.114
2458936.3252	16.814	0.061	2459214.4187	-11.000	0.250	2459271.4616	-5.222	0.238
2458936.3674	16.789	0.063	2459235.4186	-64.210	0.330	2459277.3885	-3.663	0.095
2458940.6134	7.463	0.080	2459246.5492	-21.920	0.230	2459299.5060	5.240	0.112
2458956.4440	8.543	0.061	2459266.6406	-83.720	0.270	2459303.5632	-3.143	0.098
2458957.4578	15.449	0.071	2459266.6517	-83.450	0.220	2459304.5609	0.552	0.086
2458991.3658	16.101	0.091	2459267.5547	-61.740	1.310	2459304.5827	1.008	0.051
2459002.4285	15.758	0.076	2459267.5658	-61.290	1.040	2459305.5689	19.933	0.142
2459016.5113	14.793	0.121	2459268.5710	-16.850	0.120	2459305.5906	20.017	0.217
2459035.3838	12.755	0.102	2459269.6577	5.100	0.190	2459309.5167	-3.738	0.189
2459040.4020	11.440	0.090	2459270.5375	-15.470	0.300			
2459040.4890	11.188	0.081	2459271.5028	-59.130	0.350			
2459040.5312	10.929	0.079	2459277.3644	-51.350	0.200			